CERN-ACC-NOTE-2016-0039

2016-03-30

Mikko.Karppinen@cern.ch

High Gradient Nb_3Sn Quadrupole Demonstrator MKQXF Engineering Design

C. Kokkinos
FEAC Engineering P.C., Patra, Greece
M. Karppinen
CERN, Geneva, Switzerland

Keywords: LHC, HL-LHC, FCC, high field magnet, quadrupole, Nb_3Sn

Abstract

A new mechanical design concept for the Nb_3Sn quadrupoles has been developed with a goal of an accelerator quality magnet that can be industrially produced in large series. This concept can easily be extended to any length and applied on both 1-in-1 and 2-in-1 configurations. It is based on the pole-loading concept and collared coils using dipole-type collars. Detailed design optimisation of a demonstrator magnet based on present base-line HL-LHC IR quadrupole QXF coil geometry has been carried out including the end regions. This report describes the design concept and the fully parametric multi-physics finite element (FE) models that were used to determine the optimal assembly parameters including the effects of the manufacturing tolerances.

This is an internal CERN publication and does not necessarily reflect the views of the CERN management.

HIGH GRADIENT NB3SN QUADRUPOLE DEMONSTRATOR MKQXF ENGINEERING DESIGN

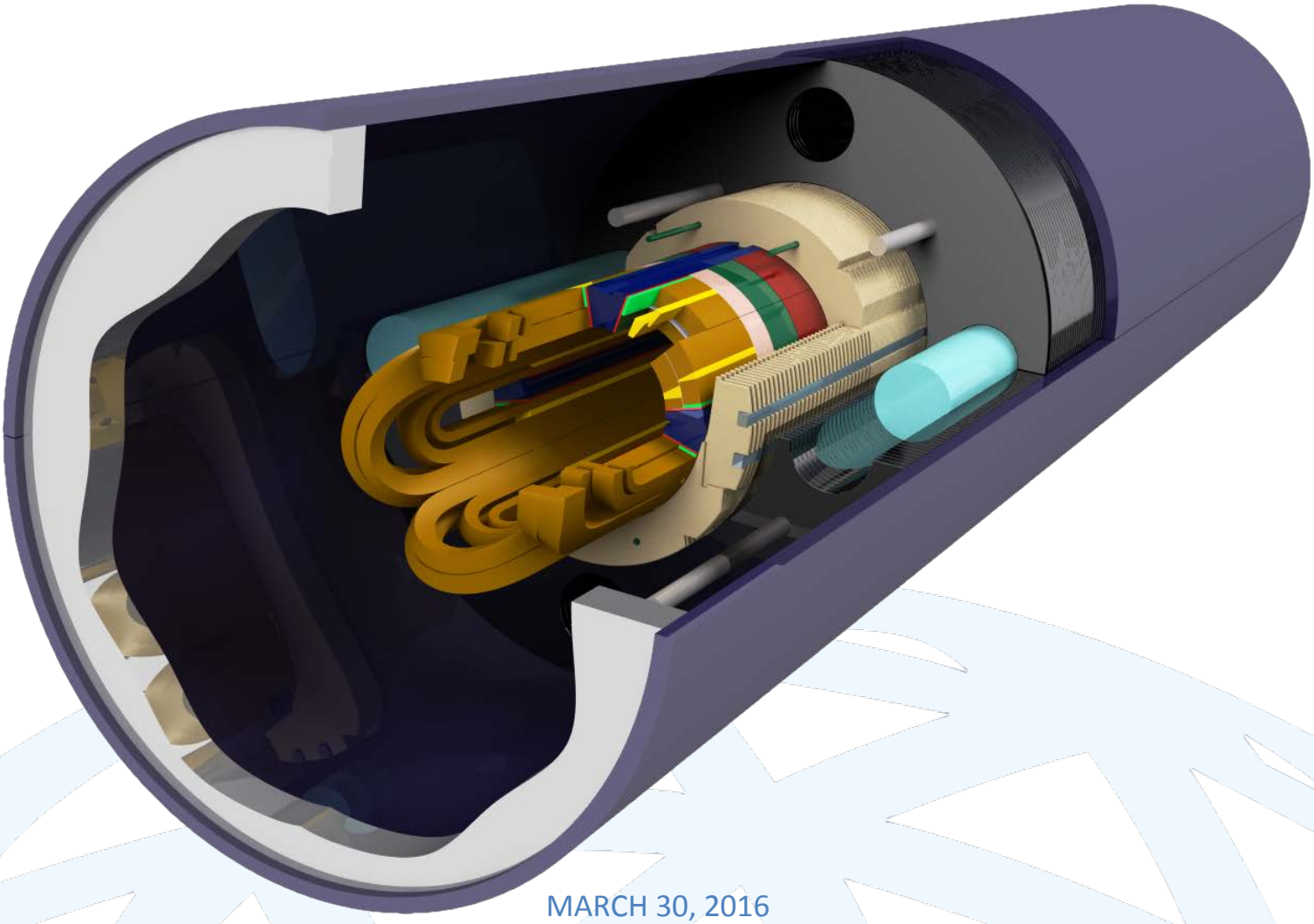

MARCH 30, 2016

FEAC ENGINEERING P.C.
www.feacomp.com – info@feacomp.com

1 Table of Contents

2 Introduction

The future upgrades of the CERN accelerator chain along with the future high-energy colliders, notably the FCC, will require high gradient quadrupoles. The most likely option for the conductor technology today is Nb_3Sn, which sets stringent requirements for the coil fabrication technology and the mechanical structure of the magnet cold mass. Any larger series of magnets shall be industrially produced whilst respecting the criteria of accelerator quality magnets in terms of the magnetic performance, reproducibility and reliability. Given the significant investment in conductor, the losses during the manufacturing process shall be minimized by careful engineering of the magnet's cold mass and the optimization of the production tools and procedures.

At CERN, a long experience from industrially produced accelerator magnets has been acquired over the years culminating in the successful series production of the LHC Main Dipoles (MB) and Main Quadrupoles (MQ) along with special magnets for the insertion regions. They all share similar well-proven features like collared coils and laminated iron yokes for clamping the Nb-Ti coils under the influence of very high electro-magnetic forces. The manufacturing methods have been well optimized over the years and significant production infrastructure exists and is fully operational at CERN for various magnet types and lengths up to 15 m. The collar and yoke laminations are typically fine-blanked with very tight tolerances at the 20 µm level, which enables very good reproducibility and manufacturing accuracy for long magnets and series production.

To address the limitations [1] of design concepts developed in the frame of the US high field magnet programs and to make use of the extensive experience of collared coils, a new concept for Nb_3Sn dipole was developed and implemented in the CERN 11T Dipole model magnets. The main difference from the US coil concept is that the Ti-alloy pole is not part of the coil, but inserted during the assembly process (Fig. 1).

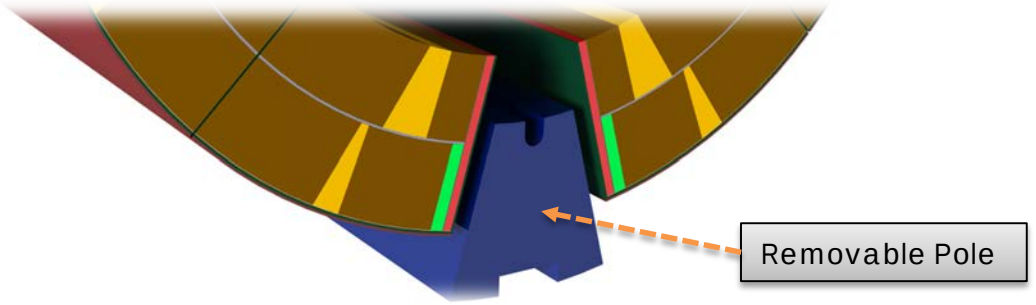

Figure 1: The removable pole in the pole-loading concept

This allows shimming at the pole and uses the collars more efficiently for creating the coil pre-stress, similarly to the collared Nb-Ti accelerator magnets and not relying on elliptic deformation of the coils. As part of the HL-LHC project, the 11 T Dipole was the first Nb_3Sn magnet designed from the beginning to be compatible with the accelerator requirements and industrial production [2]. The first 2-m-long single aperture model

magnets showed very good performance reaching the design field of 12 T and validated the pole-loading concept along with other new innovative ideas aiming to ensure the reliable operation in the accelerator environment.

The pole-loading concept has been further developed for Nb_3Sn quadrupoles. The pole region of the coils is identical to the dipole and the collared coil is based on dipole-type collars. This has some implications on the design of the pole area at the mid-plane of the top and bottom collars. The main advantage of using the dipole-type collars is that the collaring is done simultaneously over the entire coil length thus avoiding local shear stress in the coil, and the use of existing infrastructure (collaring presses) and well-known assembly procedures.

The conceptual design study was conducted at CERN in 2014, with very promising results [1].For benchmarking purposes and to compare with the present base-line design of the HL-LHC IR quadrupole QXF [3], based on bladder-and-key concept, this conceptual study was made with identical coils and quasi-identical magnetic characteristics (Fig. 2). Such design featuring 140 T/m gradient in 150 mm coil aperture is significantly more demanding mechanically than the present FCC IR Quadrupole parameters (200 T/m, 90 mm aperture) and, as such, provides the FCC optics studies an idea of the upper limit of such magnet with presently available technology. This new concept can also be easily extended for the 2-in-1 configuration of any length that will be required for the FCC main quadrupoles.

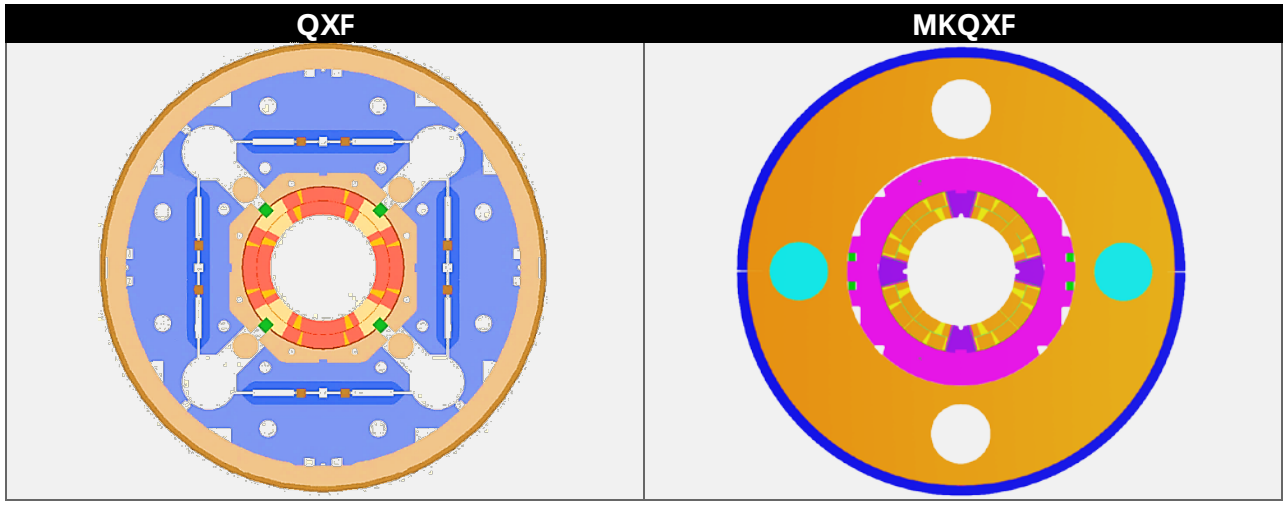

Figure 2: Cross sections of QXF & MKQXF. QXF is based on the bladder-and-key concept while MKQXF is based on the pole loading concept

This report describes the design concept and the fully parametric multi-physics finite element (FE) model that was used for the detailed design optimization. The optimized assembly parameters and the effect of the manufacturing tolerances are presented. As a result, the manufacturing drawings can easily be made from the optimized 3D CAD models followed by the procurements of all parts to launch the construction of a short demonstrator magnet.

3 Mechanical structure

3.1 Main design features

The main features of the MKQXF design illustrated in Figure 3 include:

- Epoxy impregnated Nb_3Sn coils with two winding layers.
- Filler wedges to align the pole angle of the inner and outer winding layers.
- Removable Ti-alloy pole-wedges, which at the mid-plane have a 12° taper, such that the long collars with similar taper, push the wedge radially in during the collaring process.
- 2-mm-thick stainless steel loading plates to protect the coil and to evenly distribute pressure on the pole turns.
- Ground insulation composed of 5 radial layers of 125 µm polyimide between the coil and the collaring shoe. The inner-most layer (so-called trace), that is glued to the coils, to ensure good thermal contact, includes the protection heaters and the electrical circuits for the voltage taps and the strain gauges.
- St. steel collaring shoe protecting the coils from the collars. Dipole-type collars (long and short collar) with collaring keys and pins to form the pre-assembled collar packs.
- The laminated yoke is made in two halves, with a horizontal tapered split
- Aluminum gap controllers bars located on yoke mid-plane.
- 15-mm-thick stainless steel shell

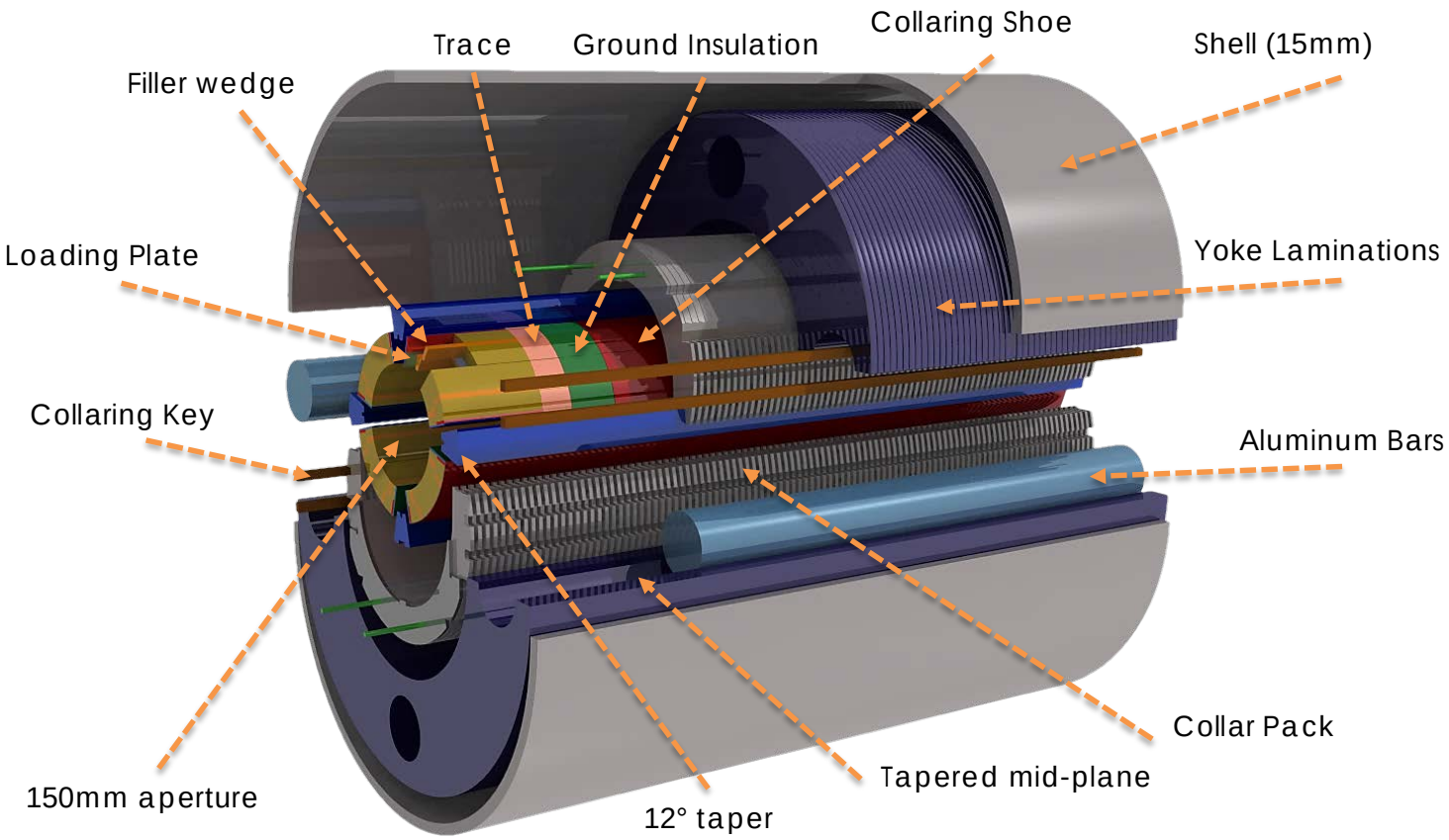

Figure 3: Exploded view of the MKQXF Nb_3Sn quadrupole showing its key features

3.2 Coil design

The two-layer coils are wound with a single length of Rutherford-type cable without an internal splice. The coil dimensions and the fabrication process are identical to the QXF coils except for the pole region. In addition, to improve the dielectric strength of the cable insulation, the combined Mica-S2-glass (similar to 11 T Dipole) may be adopted. The pole angle of the inner and outer winding layers is aligned by inserting additional filler wedge on the outer layer (Fig.4). A separate reaction pole is used during the reaction and then removed when the coil is prepared for the impregnation. To protect the coil and to distribute the pole pressure more evenly across the coil, 2-mm-thick stainless steel loading plates are added at the pole and a separate impregnation pole provides accurate size for the pole region of the impregnated coil.

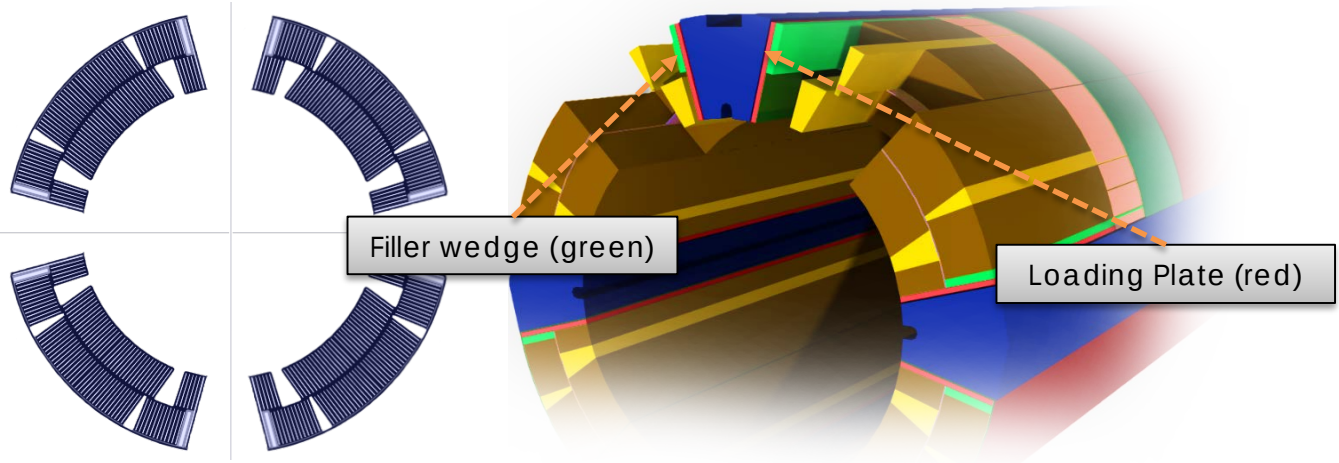

Figure 4: QXF coil adapted for pole-loading concept

In the coil ends the first end spacer, which is the extension of the pole, has a slot as shown in Figure 5. The "legs" of this spacer align with the loading plates of the straight section. A short pole wedge of 150 mm is used across this transition from straight to the end region. The pole adjustment shim shown between the collar and this short wedge is reduced by 0.2 mm further out thus reducing linearly the coil stress. This is to avoid discontinuous stress pattern in this delicate area minimizing any shear stress in the reacted Nb3Sn coils. The first end spacer has a longitudinal slit to make it more flexible. The other end spacers feature similar swivel joints in the spacer "legs" to 11 T dipole spacers to minimize the risk of insulation damage during the fabrication process. The end spacers can be made of stainless steel by selective laser-sintering (SLS) and after reaction the end saddles can be replaced by epoxy-glass (EPGC3) parts to better match the rigidity of the end region with the straight section and to make the electrical insulation of the splice region more robust.

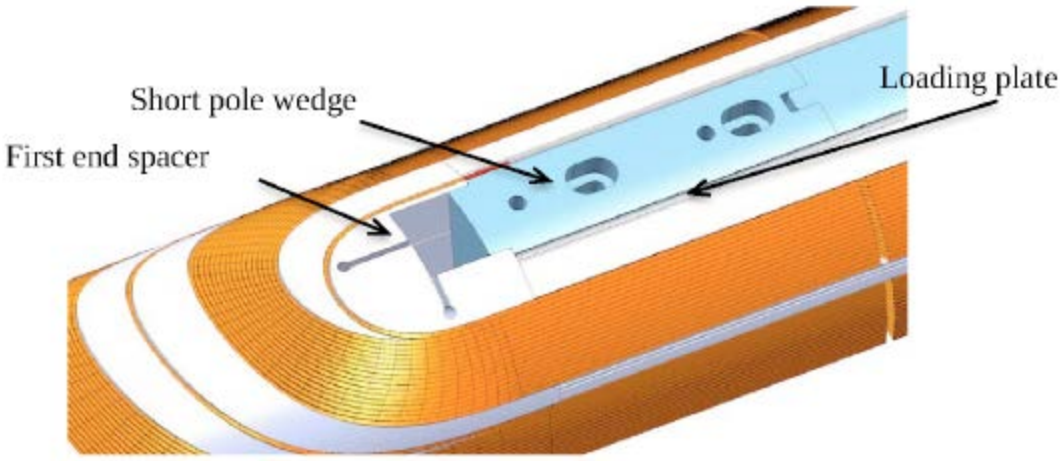

Figure 5: 11 T Dipole coil return end showing the transition between coil straight section and the end region

3.3 Collared coil

The four impregnated coils are assembled together with the appropriate ground insulation that goes around the coil mid-plane and over the loading plate at the pole. The pole wedges are then inserted in the coils, which also secures the ground insulation in place. The collaring shoes are mounted around the ground insulation prior to pre-assembling the collar-packs. The collaring press (Fig. 6) has five contact areas with each collar, and pushes the upper collar pack towards the lower until the key-ways are aligned to allow the insertion of the narrow face of the tapered keys. Once the keys have been pushed in, the press is released and the collared coil held together by the keys.

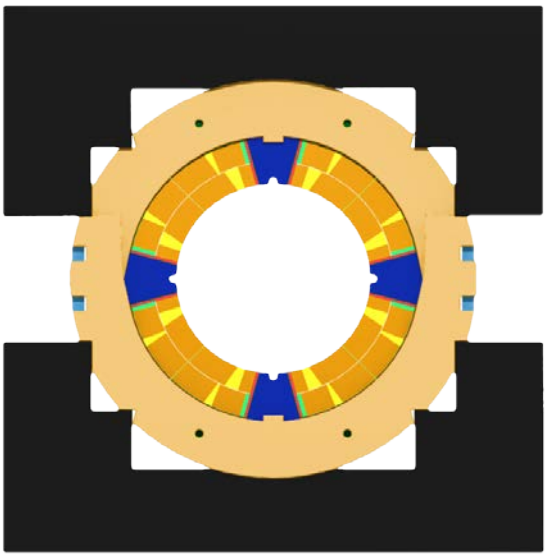

Figure 6: Under Collaring Press

The pole wedges in the vertical axis are similar to the 11 T Dipole pole wedges with the alignment slot that locates the collar nose and transmits the vertical force from the collars to the pole wedge. In the horizontal plane the pole wedge has a 12° taper such that the long collars with similar taper near the horizontal plane push the wedge radially in during the collaring (Fig. 7). The stress relief notch in the pole wedges is essential for the stress distribution of the inner layer pole-turns.

On the outer radius the short collar is 0.5 mm smaller than the long collar. Therefore, the short collars can be considered essentially as fillers except for the mating plane region, where they contribute to the lateral rigidity of the collared coil.

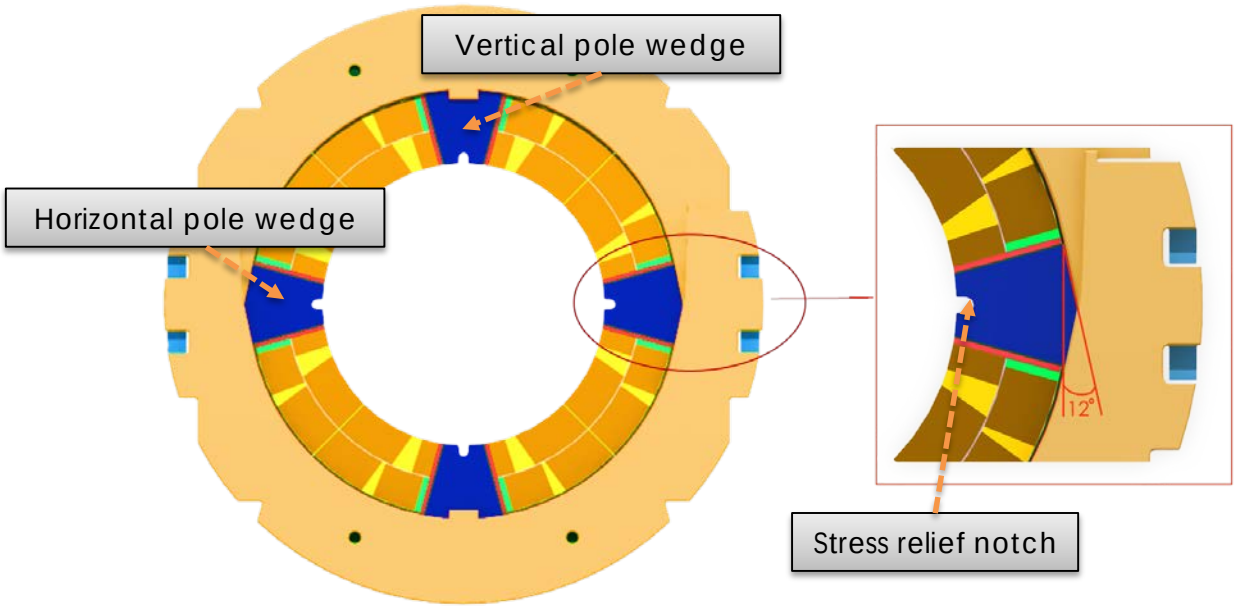

Figure 7: Collared Coil

3.4 Yoke and Shell

The laminated iron yoke, with an outer diameter of 600 mm, is made of two halves with a horizontal split (Fig. 8). The yoke inner diameter has line-to-line fit with the nominal collar outer contour. The yoke mid-plane is tapered such that with the contact on the inner radius the outer radius has a 0.05 mm gap in the free state. This provides some elasticity to the yoke to store strain energy against the enormous Lorentz forces from the coils.

In single aperture quadrupoles operating at superfluid helium one or two heat exchanger tubes typically run through the yoke. For symmetry reason two additional holes are added in the yoke laminations and can be used for mechanical purposes by inserting Al-bars or thick-walled tubes. By appropriately dimensioning, the differential thermal contraction of the yoke, the collared coil and the Al-bars shall be accounted for such that the yoke gap is closed at cryogenic temperature and contact at the collar-yoke interface is preserved. This requires the yoke gap to remain slightly open at ambient temperature.

An open gap is very difficult to be accurately controlled during the yoke assembly in the powerful welding press and it is better to press against a known reference plane (displacement control instead of force/pressure control). The Al-bars act as gap controller allowing an accurate adjustment of the yoke gap during the assembly phase and protecting the coil from over-compression. During the cool down the gap controller then shrinks away from the iron allowing the closure of the gap and hence ensuring static and rigid envelope around the collared coil. At cryogenic temperature, the yoke gap shall remain closed. This creates a very rigid structure to

sustain the magnetic forces and to avoid coil deformation that can have deleterious effect on quench performance and field quality.

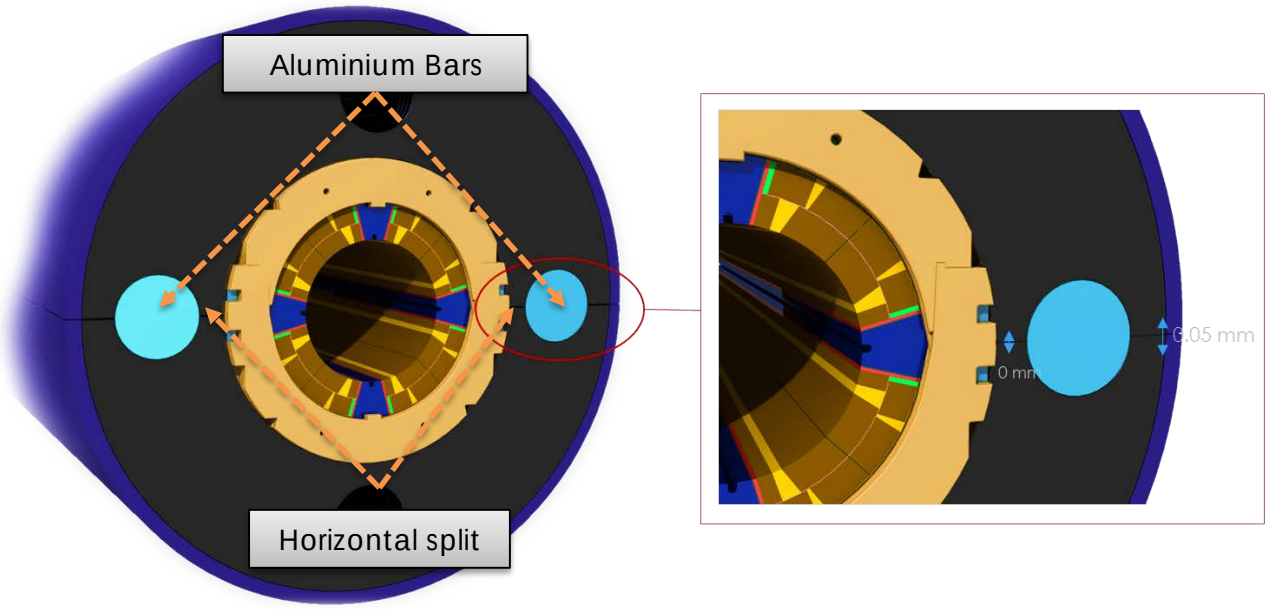

Figure 8: Horizontal split on the yoke and shell

The 15-mm-thick stainless steel outer shell is made in two halves and welded around the yoke in the welding press. Weld shrinkage of up to 1mm can be obtained with present welding techniques and typically the mean shell tension is kept below 200 MPa at the ambient temperature. The shell is welded at the mid-plane.

3.5 Shim locations

The pole-loading concept allows the tailoring of the coil pre-compression to counter-balance the effects of the electromagnetic forces and to minimize the stress gradients across the brittle Nb_3Sn coils. The experience with the 11 T model magnets has also proven the compensation of the dimensional distortions (up to several tenths of mm) of the coils by shimming. The shim locations considered in this study are shown in Figure 9.

The pole and mid-plane shims are primarily used for the adjustment of the pre-stress and the radial shim between the collar and the coils can be used to compensate for the dimensional differences of the coils. In addition, the adjustment shim between the pole wedge and the collar can be used at the model phase to adjust the pre-loading by adjusting the radial position of the wedge relative to the coil without taking the coil assembly apart. These shims would not be used once a good dimensional reproducibility of the coils has been reached. There is a shim between the collared coil and the yoke that provides positive and negative adjustment of this interface. The contact area can also be limited to cover only part of the circumference, if necessary.

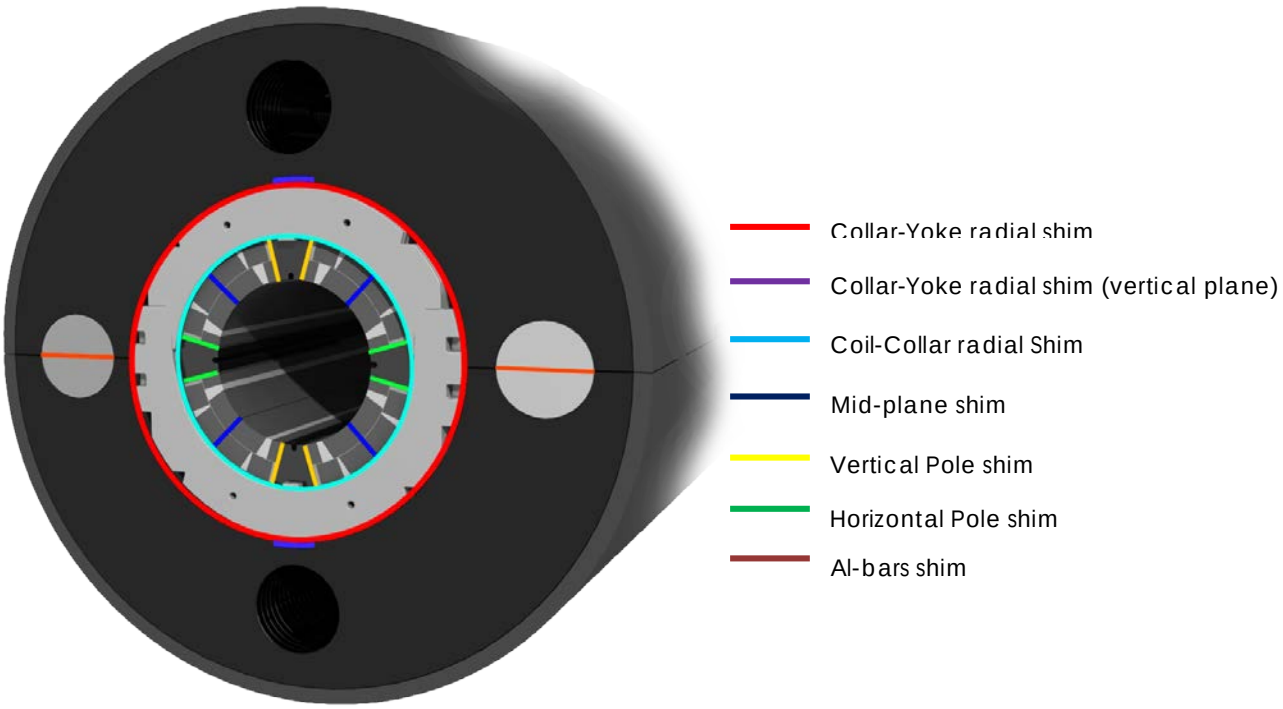

Figure 9: Shim locations

4 Design Goals

The design goals of MKQXF are summarized below:

1. The coils shall be solidly clamped to minimize any dimensional distortions and conductor movements. The maximum value for the acceptable coil stress is still a subject of debate in the magnet community, but keeping it below 165 MPa at all times is generally considered safe.
2. The stress distribution and deformation of the coils shall be symmetric, minimizing the stress gradients especially at the pole regions. The distortions from the quadrupole symmetry shall be minimized.
3. During collaring, the press shall provide the necessary vertical displacement to allow the insertion of the tapered keys into the keyways. The collars are dimensioned to provide most of the coil pre-stress in a well-controlled fashion during collaring with minimum spring-back and elliptical deformation.
4. The Al-bars inserted in the mid-plane holes determine the yoke gap during the assembly phase and after the welding of the outer shell. The yoke gap shall close during the cool down and remain firmly closed up to the ultimate design gradient of 155 T/m.
5. Weld shrinkage of up to 1mm can be obtained with present welding techniques and the stainless steel outer shell tension shall be kept below 230 - 250 MPa at the

ambient temperature, depending on the steel grade.

6. At the pole regions the Lorentz forces are unloading the coil from the poles. Contrary to the coils with integrated poles, the pole-loading concept is not expected to show degradation even in the case of complete unloading, as the pole is not bonded to the coils. For modeling reasons, however, for this FEA the maximum allowed tensile stress at the pole turns was set to 10 MPa.

5 2D Model

5.1 Electromagnetic analysis

The electromagnetic model was analyzed in MAXWELL, to transfer the electromagnetic forces to the structural analysis model. The distribution and magnitude of the magnetic field was in very good agreement with ROXIE [4] & PITHIA [5] results. The mesh on the conductors is very dense and a non-linear BH-curve is used to describe the magnetization of the yoke. The magnetic field at 140 T/m & 155 T/m is shown in Figure 10 and 11.

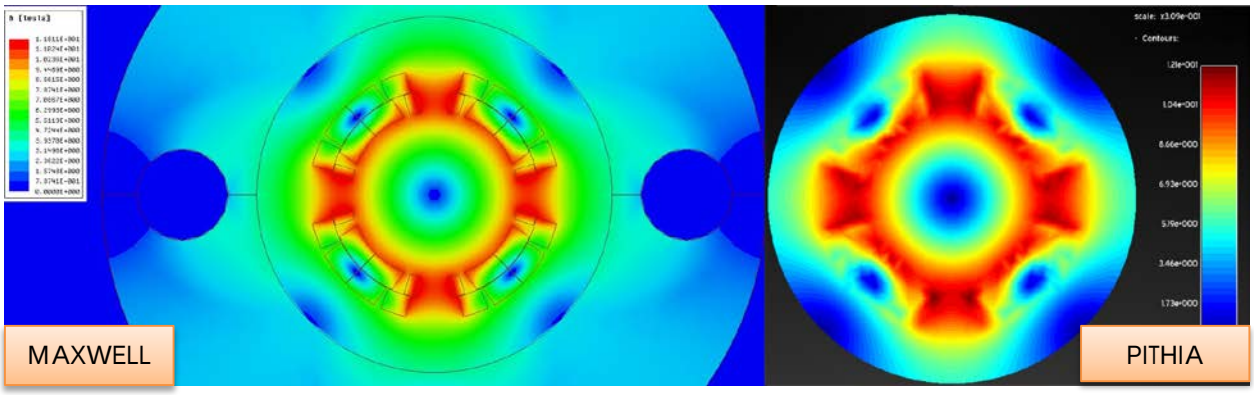

Figure 10: At 17.3 kA, 140 T/m. Maxwell 11.81 T, PITHIA 12.1 T

At 17.3 kA the coil peak field in MAXWELL is 11.81 T corresponding to a gradient of 140 T/m (nominal design gradient) (Fig. 10).

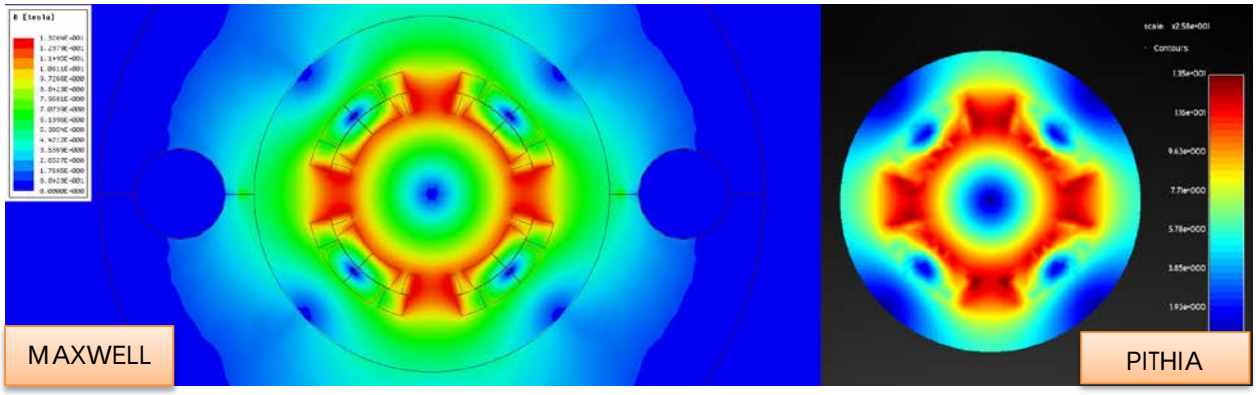

Figure 11: At 19.25 kA, 155 T/m. Maxwell 13.26 T, PITHIA 13.5 T

At 19.25 kA the coil peak field in MAXWELL is 13.26 T corresponding to a gradient of 155 T/m (ultimate design gradient) (Fig. 11). The electromagnetic forces were

transferred using the ANSYS Workbench environment and all nodes from the MAXWELL model were mapped on the structural mesh (Fig. 12).

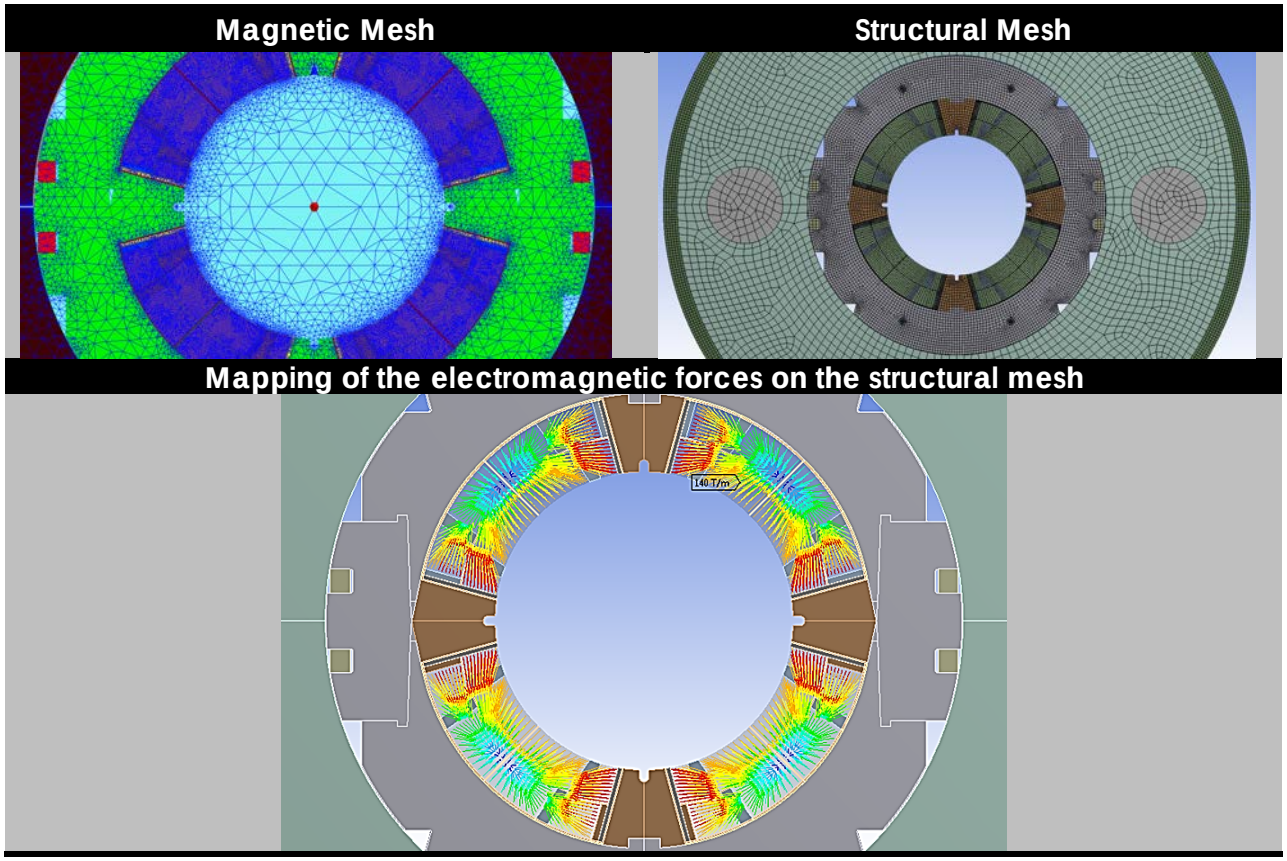

Figure 12: Mapping of the electromagnetic forces on the structural mesh

5.2 Structural Analysis

5.2.1 Finite element model

The multi-physics model combines advanced CAD tools with Finite Element Analysis (FEA) software, in the integrated design environment of ANSYS® Workbench (Fig. 13) [6].

The fully parametric FE model was created in ANSYS Mechanical accompanied by APDL macros. Higher order, 8-node, 2-D elements (PLANE 183) were used to create the mesh [7]. All parts have a thickness of 1mm except for the collars, which were defined at 0.5 mm. The collars were modeled as two overlapping layers consisting each of a long and a short collar. The contact areas were modeled with CONTA172 and TARGE169 elements with asymmetric behavior and augmented Lagrange formulation. All shims are simulated by gap elements.

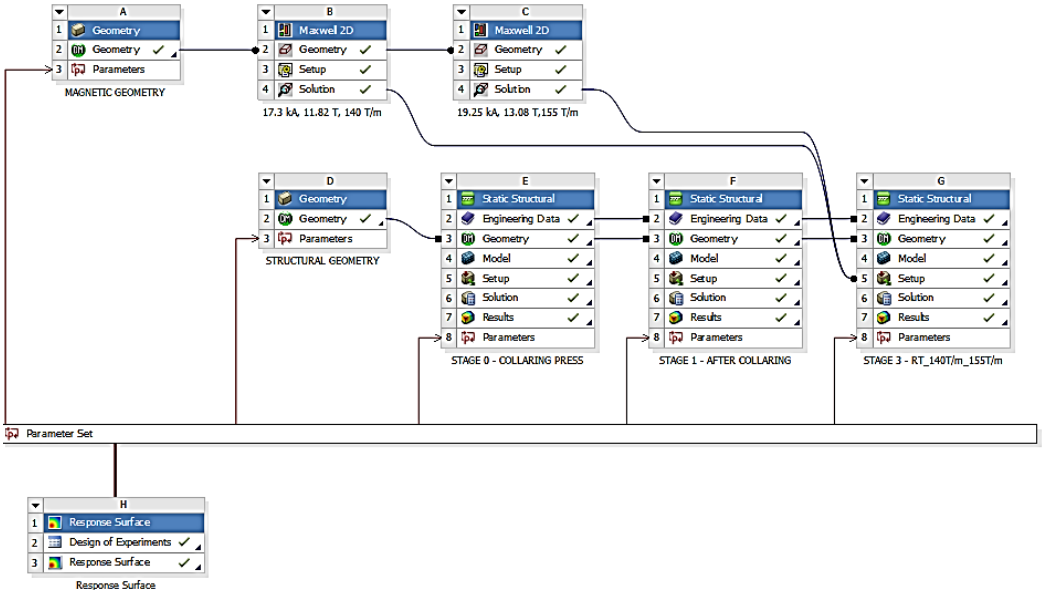

Figure 13: The 2D multi-physics model in ANSYS Workbench

The coil block, including the windings, the wedges, the interlayer insulation and the trace were modeled as a multi-body part (Fig. 14), hence no contacts were required since all nodes were merged. Bonded contact was used in the filler wedge-coil and the loading plate-coil interfaces [8]. Sliding contact was used at the ground insulation – collaring shoe interface. Frictional contact has been used elsewhere, with a friction coefficient of 0.2 (0 in the case of the frictionless model). The carefully determined contact parameters and the fine mesh ensured rapidly converging model and minimal numerical errors.

Figure 14: Coil block modeled as multi-body part

The interface between the yoke and the collared coil was modeled with 0.4 mm nominal shim. The yoke assembly step is modeled at two stages. First the yoking press (Fig. 15) is included in the FE model with a vertical displacement applied on its top and bottom faces. The second stage after completion of the cold mass assembly is modeled by applying the weld-shrinkage as forced displacement on the mating faces of the half shells. The design of the yoking press is the same as the one used in the similar FEA of the 11T Dipole. It can be seen in Fig. 15, 18, 31& 33 that there are only minor changes in the coil stress and the contact pressure at the collar – yoke and Al-bars – yoke interfaces. Therefore, only the results of second stage after the outer shell welding are included in this report.

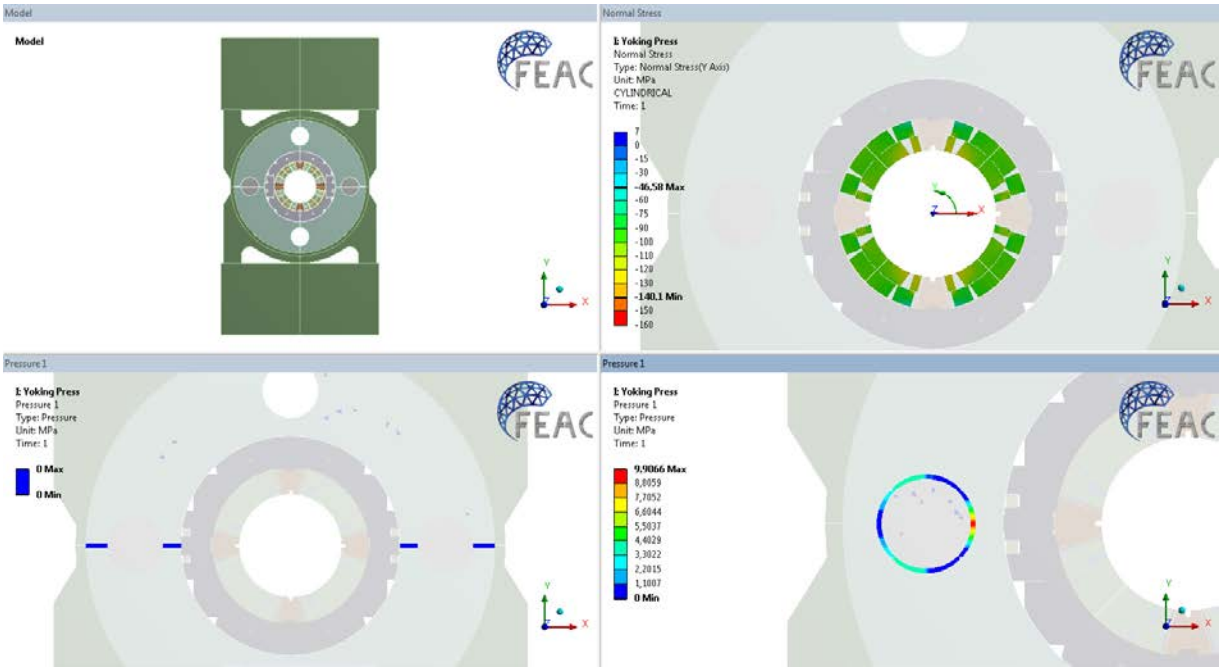

Figure 15: The yoking press has minor effect on the coil stress and the contact pressure at the collar – yoke and Al-bars – yoke interfaces

5.2.2 Material Properties

The coil material properties used in MKQXF are identical to the ones used in the QXF model, and the 11T Dipole model regarding the rest mechanical structure. All parts have been modeled with isotropic properties except for the winding blocks of the coil which are modeled with anisotropic material properties (Table 1, Fig. 16).

Part	Material	E-Modulus [GPa] 293K	E-Modulus [GPa] 4.2K	Coefficient of thermal expansion [K^{-1}]	Poisson's Ratio 293K	Poisson's Ratio 4.2K
Coil	Combination	E_x=52 E_y=44	E_x=52 E_y=44	ax= 1.07e-5 ay= 1.16e-5	0.3	0.3
Wedge	Aluminum Bronze	110	120	1.08e-5	0.3	0.3
Interlayer Insulation	G10	30	30	2,44e-5	0.3	0.3
Loading Plate	St. Steel	193	210	9.83e-06	0.28	0.28
Trace	G10	30	30	2,44e-5	0.3	0.3
Ground Insulation	G10	30	30	2,44e-5	0.3	0.3
Collaring Shoe	St. Steel	195	215	9.215e-06	0.3	0.3
Pins	St. Steel	195	215	9.897e-06	0.3	0.3
Keys	St. Steel	190	210	9.01e-06	0.3	0.3
Collars	St. Steel	195	215	9.215e-6	0.3	0.3
Yoke	Magnetic Steel	210	225	6.894e-06	0.3	0.3
Bars	Aluminum	70	79	1.45e-5	0.34	0.34
Shell	St. Steel	195	215	9.897e-06	0.3	0.3

Table 1: Values of material properties used in the model

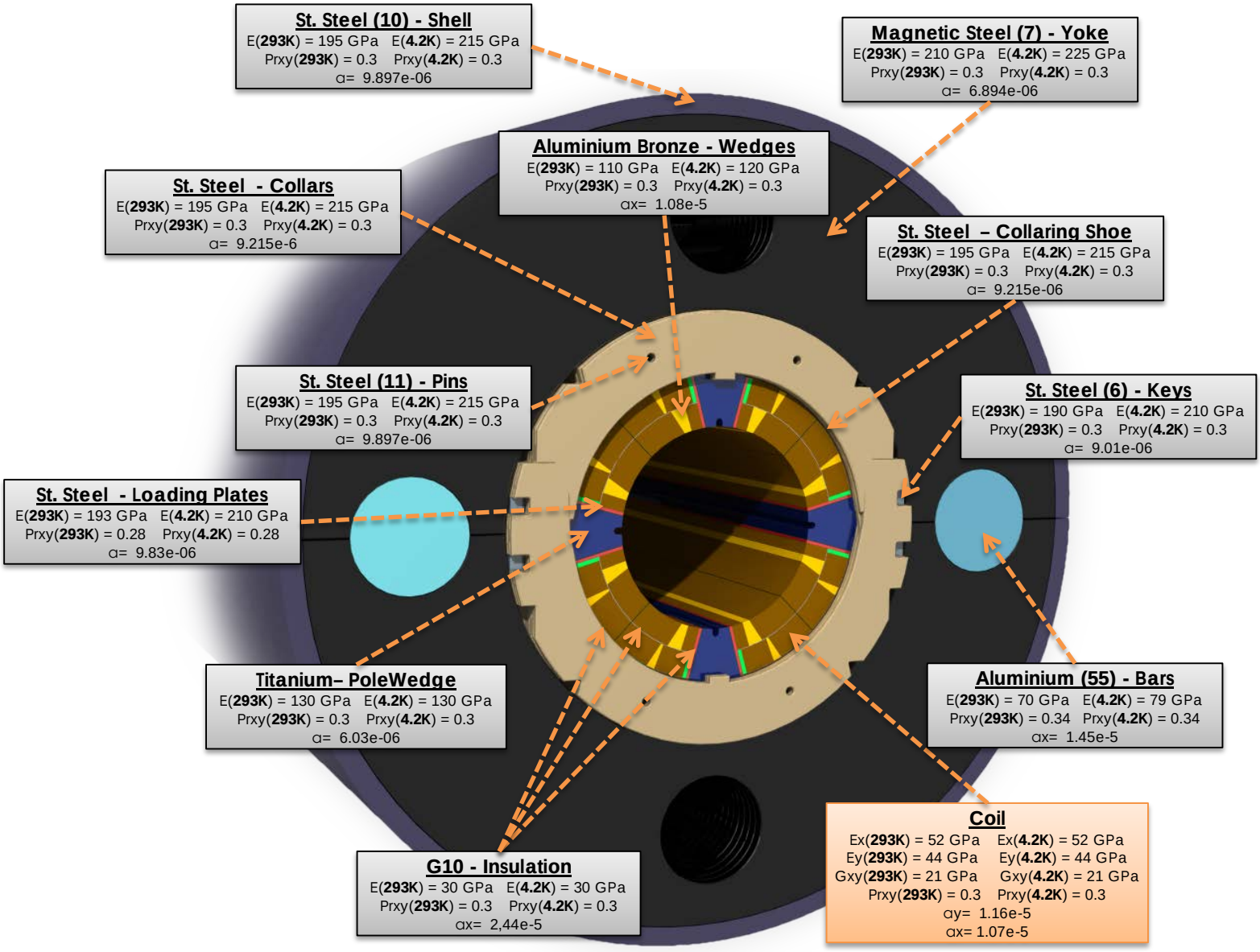

Figure 16: Material properties of the components

5.2.3 Load Steps

Six load-steps were considered in the Finite Element Analysis (FEA):

1. Under collaring press with key-ways aligned to insert the keys.
2. Collared coil.
3. Yoke assembly at 293 K.
4. At 4.2 K.
5. At 4.2 K, 140 T/m.
6. At 4.2 K, 155 T/m.

5.2.4 Results

5.2.4.1 Assembly parameters

The design study converged to the shim thicknesses listed below. The assembly parameters shown in Table 2 ensure that the design goals mentioned above, are met at all times.

Interface	Direction	Thickness [mm]
Vertical Poles – Loading Plate	Azimuthal	0.22
Horizontal Poles – Loading Plate	Azimuthal	0.15
Mid-plane	Azimuthal	0.28
Collars - Yoke	Radial	0.38
Collars - Yoke (Vertical Plane)	Radial	0.41
Weld Shrinkage	Vertical	0.96

Table 2: Optimized assembly parameters

5.2.4.2 Coil

5.2.4.2.1 Azimuthal Stress

The azimuthal coil stress evolution for the six load steps is presented in Figure 17 and Table 3. Under the collaring press, the peak stress is -112 MPa in the inner layer, near the vertical pole wedge. After releasing the press, the spring back and stress re-distribution reduces the coil stress by about 25 MPa. The yoke assembly increases the coil compression by about 47 MPa. During cool down to 4.2K, the collared coil contracts more than the yoke and the pre-compression is reduced by about 27 MPa. At 140 T/m & 155 T/m the very rigid structure keeps the stress distribution very uniform, inside the safe stress levels. At 155 T/m the coil stress at the poles is 4 MPa in tension. At the coil mid-plane, the maximum stress on the inner layer ranges from -136 to –156 MPa at 155 T/m.

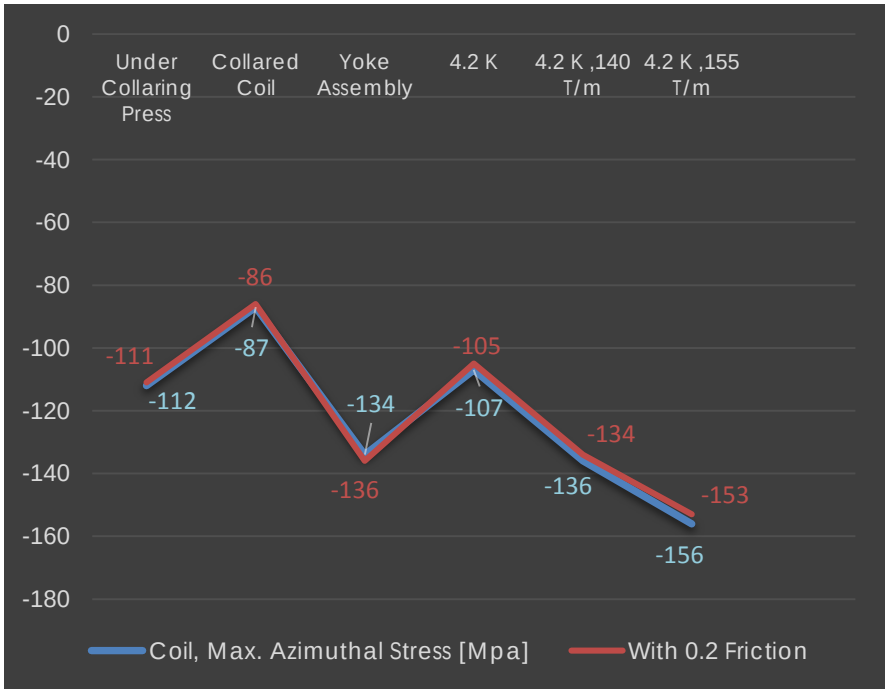

Figure 17: Coil stress [MPa] evolution

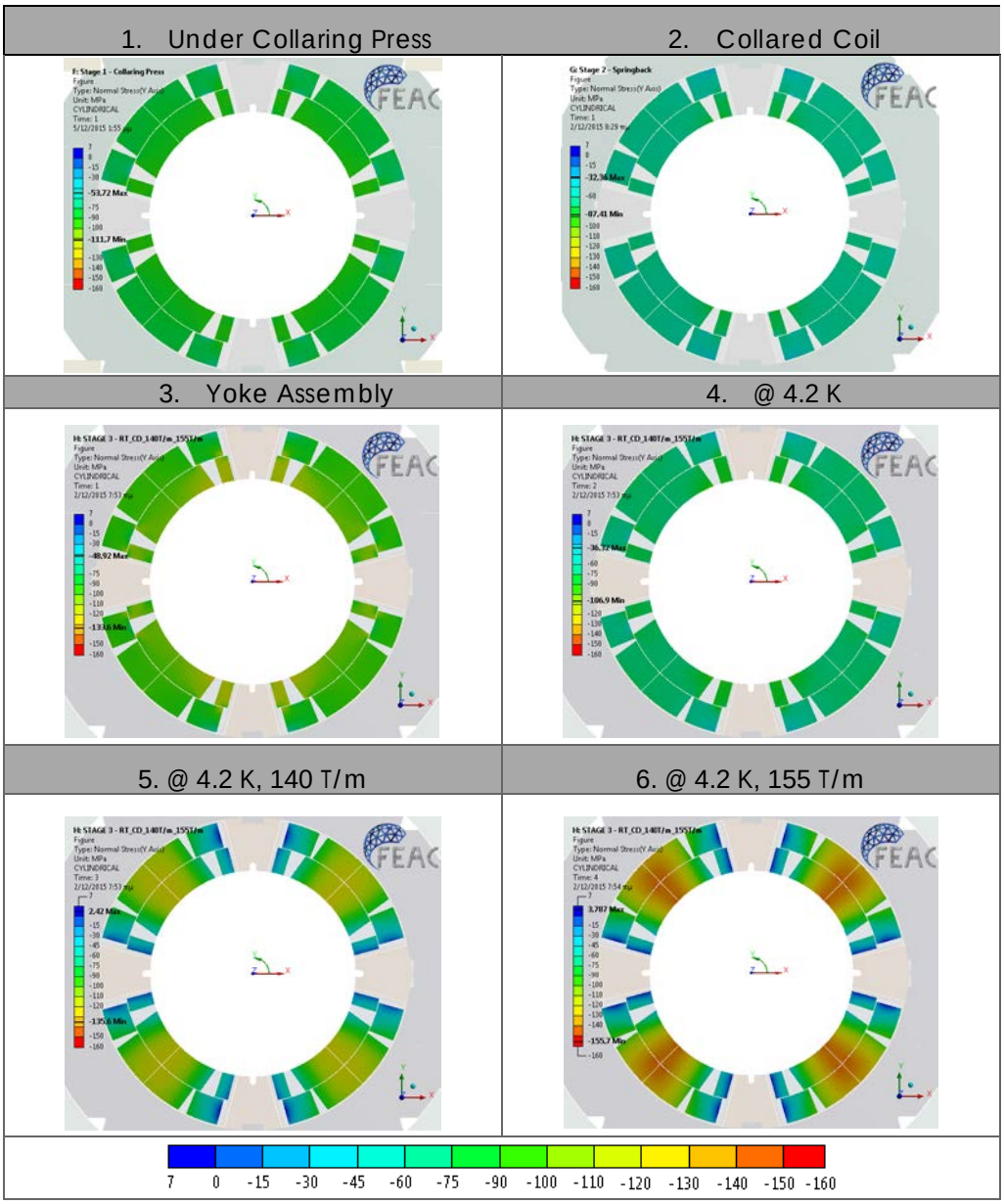

Figure 18: Coil Stress [MPa] evolution for the six load steps

Figures 18-21 illustrate the azimuthal coil stress evolution for the six load steps. After collaring and after shell welding, the stress at the horizontal and vertical pole has a maximum difference of about 10 MPa. As the yoke gap is slightly open at RT, there is still a slight asymmetry in the stress distribution of the coils. After the cool down, the yoke gap is firmly closed and the stress distribution is almost perfectly symmetric in the coils. The poles have highest and the mid-plane lowest pressure to counter-balance the Lorentz forces. It can also be seen that the stress distribution across the coils is very uniform at all stages, which is particularly important in the pole regions that see largest stress variation of in operating conditions.

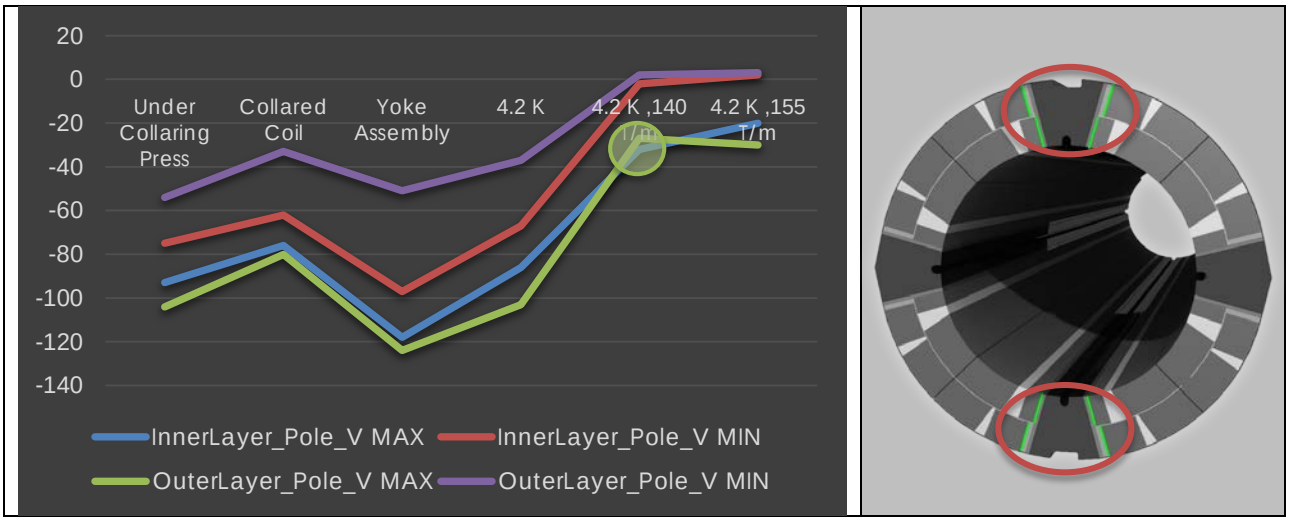

Figure 19: Azimuthal stress [MPa] in the vertical pole region

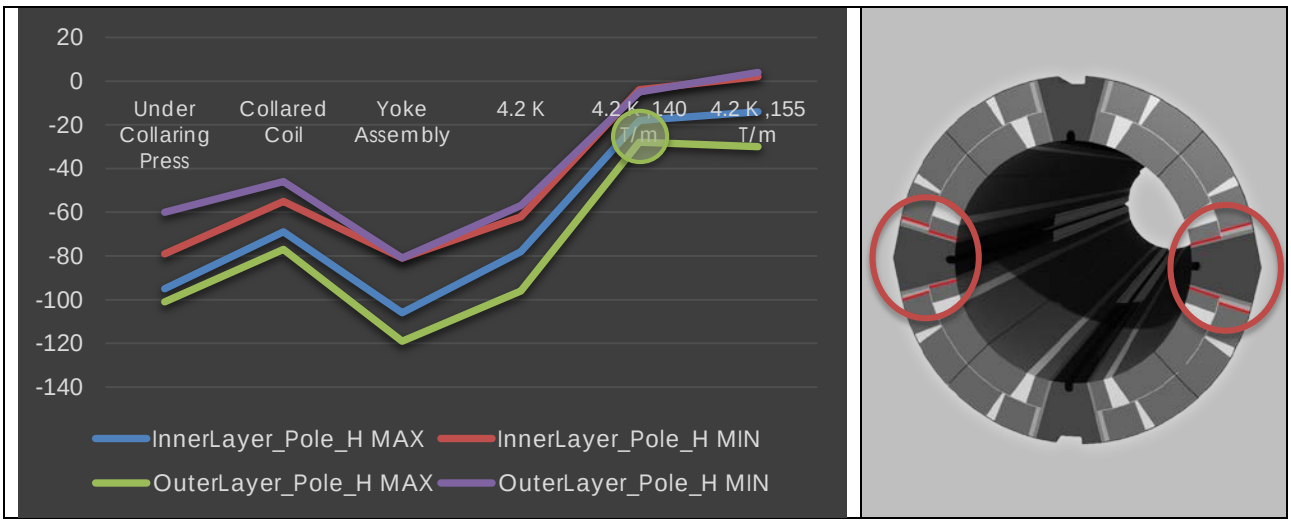

Figure 20: Azimuthal stress [MPa] in the horizontal pole region

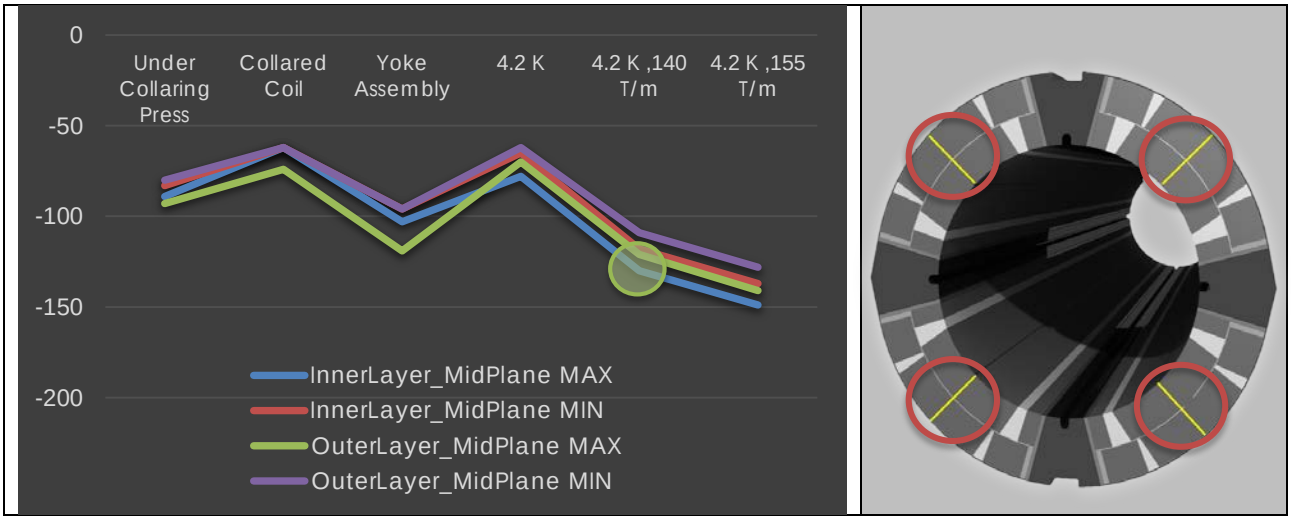

Figure 21: Azimuthal stress [MPa]at the coil mid-plane

5.2.4.2.2 Radial Deformation

The design goal is to achieve a symmetric deformation of the vertical and the horizontal pole turns during cool down, to prevent any distortions from quadrupole symmetry. Figure 22-23 shows the radial deformation of the coil. Under press the coil assembly deforms elliptically outwards along the horizontal axis, while after spring back the elliptic deformation is along the vertical axis. After the yoke assembly the yoke gaps is slightly open and determined by the Al-bars and hence some elliptic deformation remains visible in the coils. During cooling down the yoke gap is firmly closed restoring the circular symmetry of the coil assembly. During excitation the horizontal pole turns are solidly clamped, however, there is some radial deformation on the vertical pole turns, which can probably be reduced by further optimization of the assembly parameters.

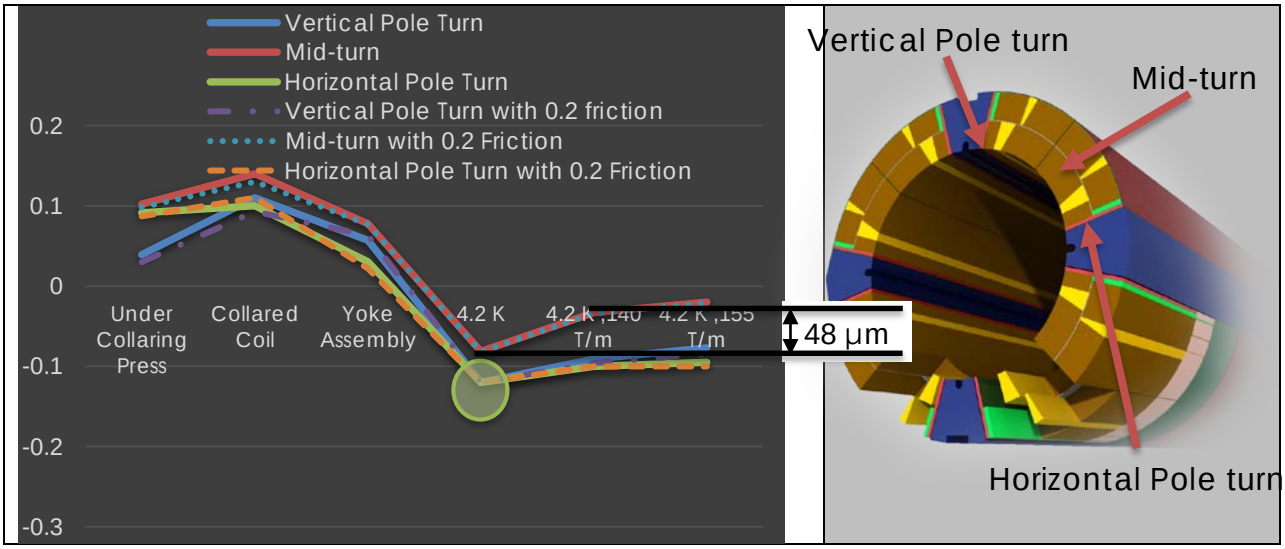

Figure 22: Radial deformation [mm] of coil, inner layer

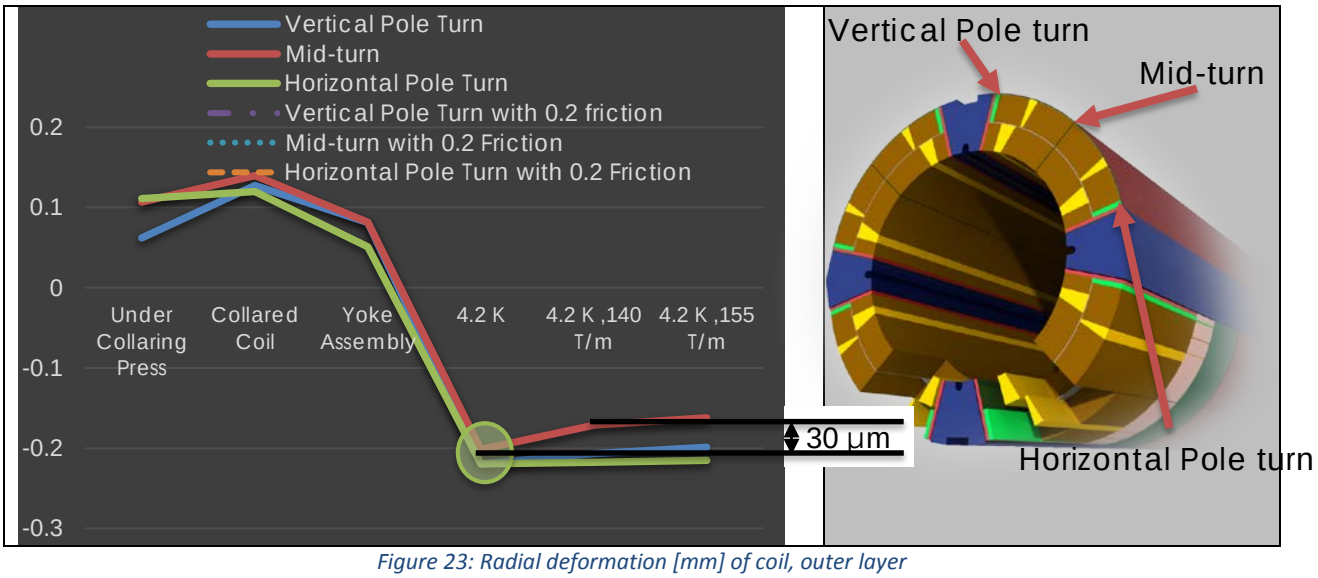

Figure 23: Radial deformation [mm] of coil, outer layer

5.2.4.3 Reaction Forces

The reaction forces help understanding the interaction between parts and the pressure applied at their interfaces. The contact area and contact pressure of the key radial interfaces are presented in Figure 24. The relative magnitude of the reaction is given by the arrow length.

1. Under Collaring Press	2. Collared Coil
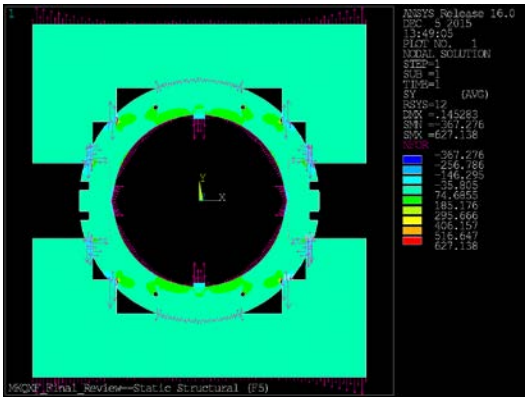	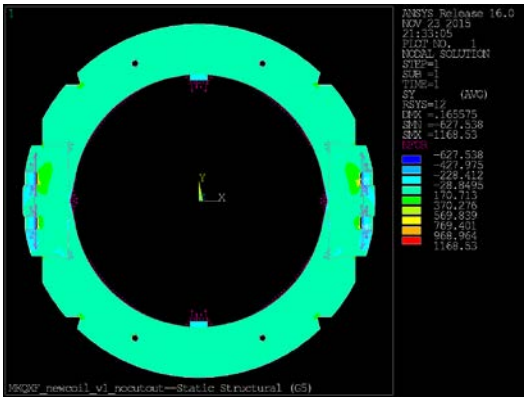
3. Yoke Assembly	**4. @ 4.2 K**
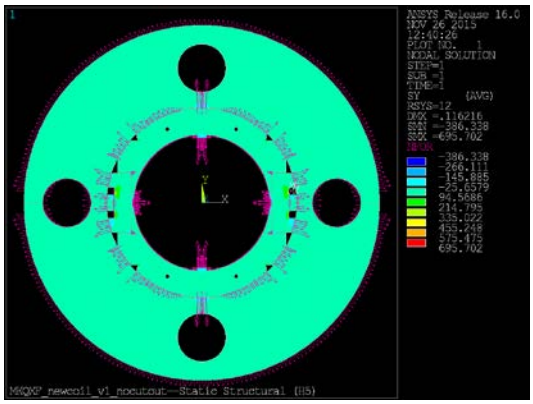	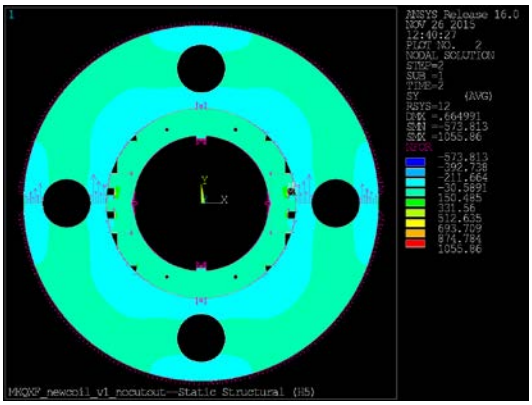
5. @ 4.2 K, 140 T/m	**6. @ 4.2 K, 155 T/m.**
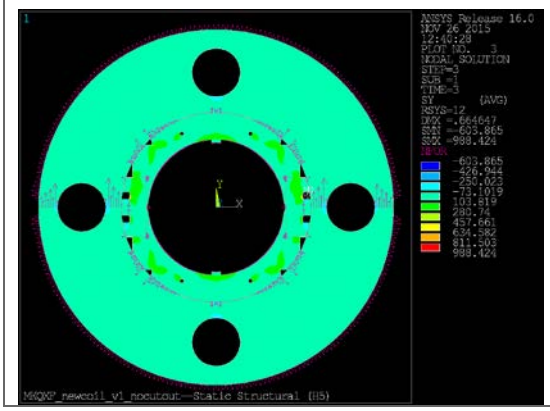	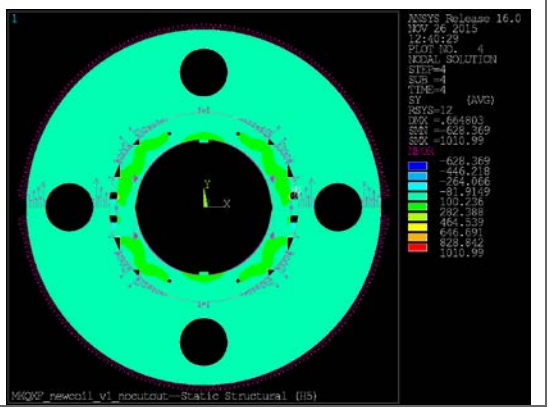

Figure 24: Evolution of reaction forces at all stages

5.2.4.4 Collars

5.2.4.4.1 Von-Mises Stress

The areas around the keys indicated in grey color in Figure 25 typically plastify due to the stress concentration. Except for these areas, the stress level in the collars stay well within the elastic zone at all time, as illustrated in Figure 26.

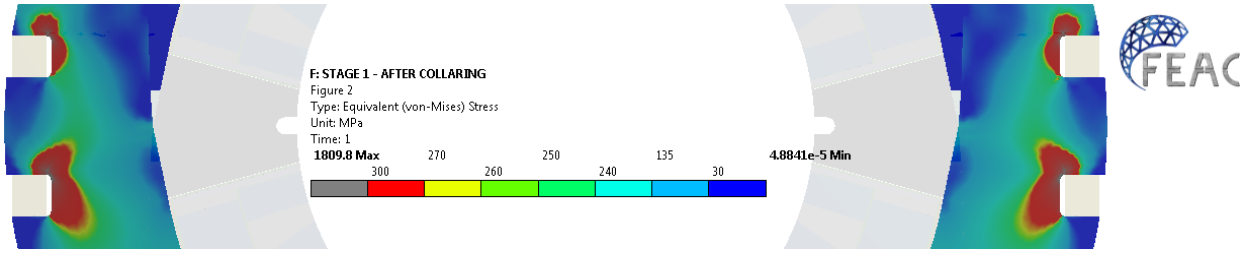

Figure 25: Equivalent stress [MPa] around the collaring keys after collaring

1. **Under Collaring Press**	2. **Collared Coil**	3. **Yoke Assembly**
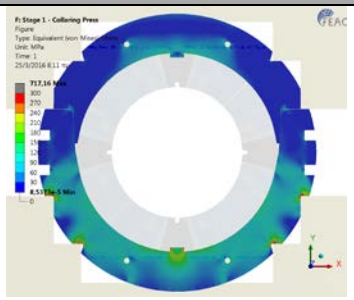	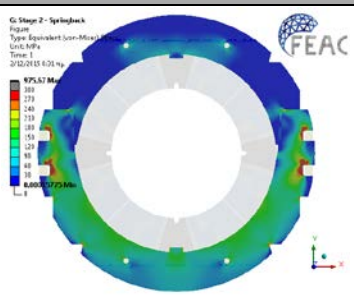	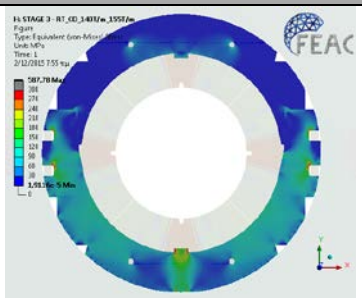
4. **@ 4.2 K**	5. @4.2 K, 140 T/m	6. @4.2 K, 155 T/m
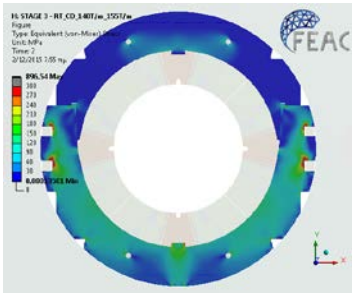	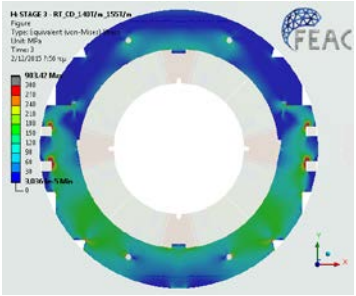	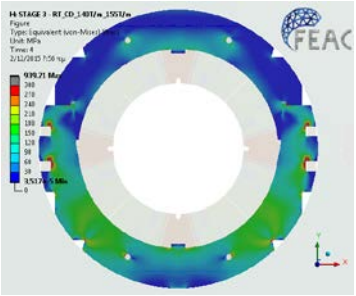

Figure 26: Equivalent collar stress [MPa] at all stages

5.2.4.4.2 Radial Deformation

The evolution of the radial displacement of the collar outer radius along the horizontal and vertical axis relative to the nominal (free) dimensions is shown in Figure 28. At the ambient temperature one can observe the slightly ovalised shape along the vertical axis. After cool

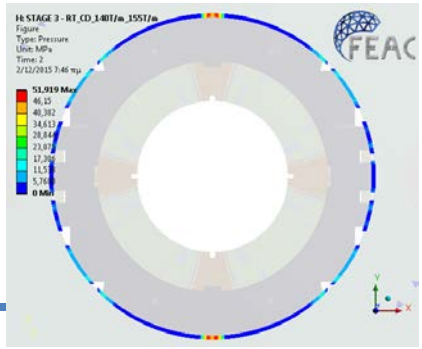

Figure 27: Contact pressure at 4.2 K

down the circular symmetry is restored and the contact pressure at the collar-yoke interface reaches the maximum value on the vertical plane (Fig. 27) due to the deformation of the yoke laminations.

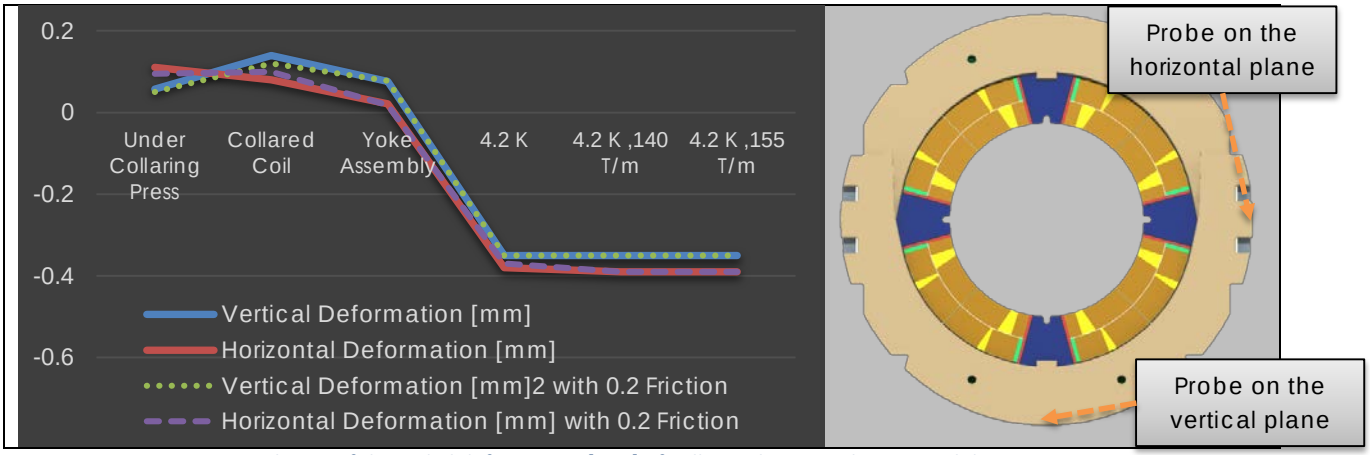

Figure 28: Evolution of the radial deformation [mm] of collars relative to the nominal dimension at 293 K

During powering the horizontal split yoke provides somewhat less support for the coils and some horizontal deformation can be observed, whereas in the vertical plane such deformation is not present up to 155 T/m.

5.2.4.5 Yoke

The general rigidity of the yoke laminations is reduced by the heat exchanger holes and the horizontal split plane. During the yoke assembly the interference between the collared coil and the yoke around the vertical axis induce slight bending of the yoke lamination around the collared coil. To compensate for this and to store the strain energy in the yoke the mid-plane has a slight taper. Along the horizontal plane the contact pressure at the collar-yoke interface is enough to bend the region between the heat exchanger hole that locates the Al-bar and the collared coil.

5.2.4.5.1 Von-Mises Stress

The equivalent stress evolution illustrated in Figures 29 and 30 indicate comfortable levels at all times.

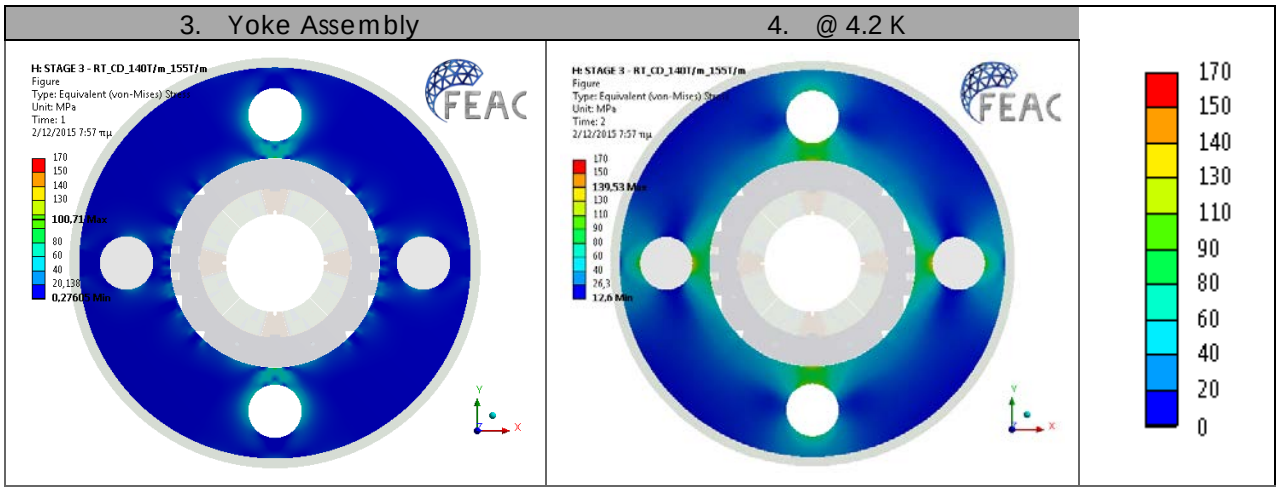

5. @ 4.2 K, 140 T/m	6. @4.2 K, 155 T/m	
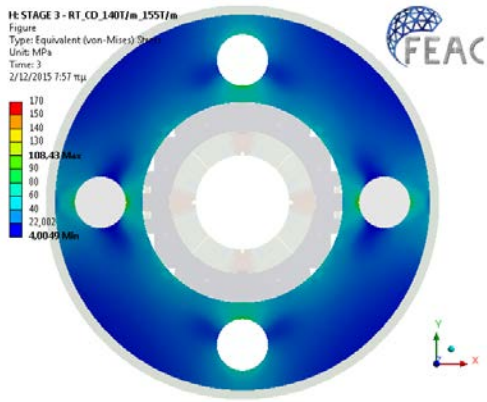	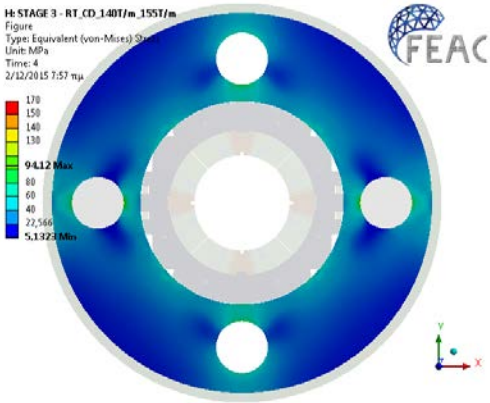	

Figure 29: Equivalent yoke stress [MPa] at all stages

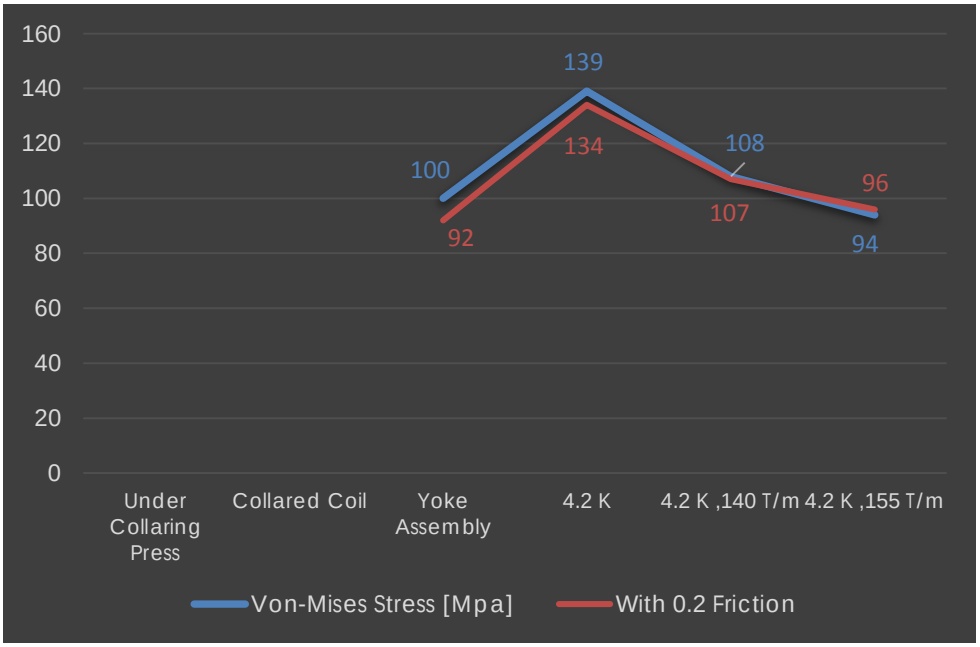

Figure 30: Equivalent yoke stress [MPa] evolution

5.2.4.5.2 Contact Pressure at the tapered horizontal split of the yoke

At ambient temperature, the yoke gap is defined by the Al-bars (Fig. 33), while at cryogenic temperature the gap is firmly closed, starting from the inner diameter towards the outer (Fig. 31). As discussed above, the slight bending of the yoke laminations results in higher contact pressure on the inner side of the Al-bars. The yoke gap remains closed up to 155 T/m creating a rigid envelope for the collared coil to sustain the very high electromagnetic forces.

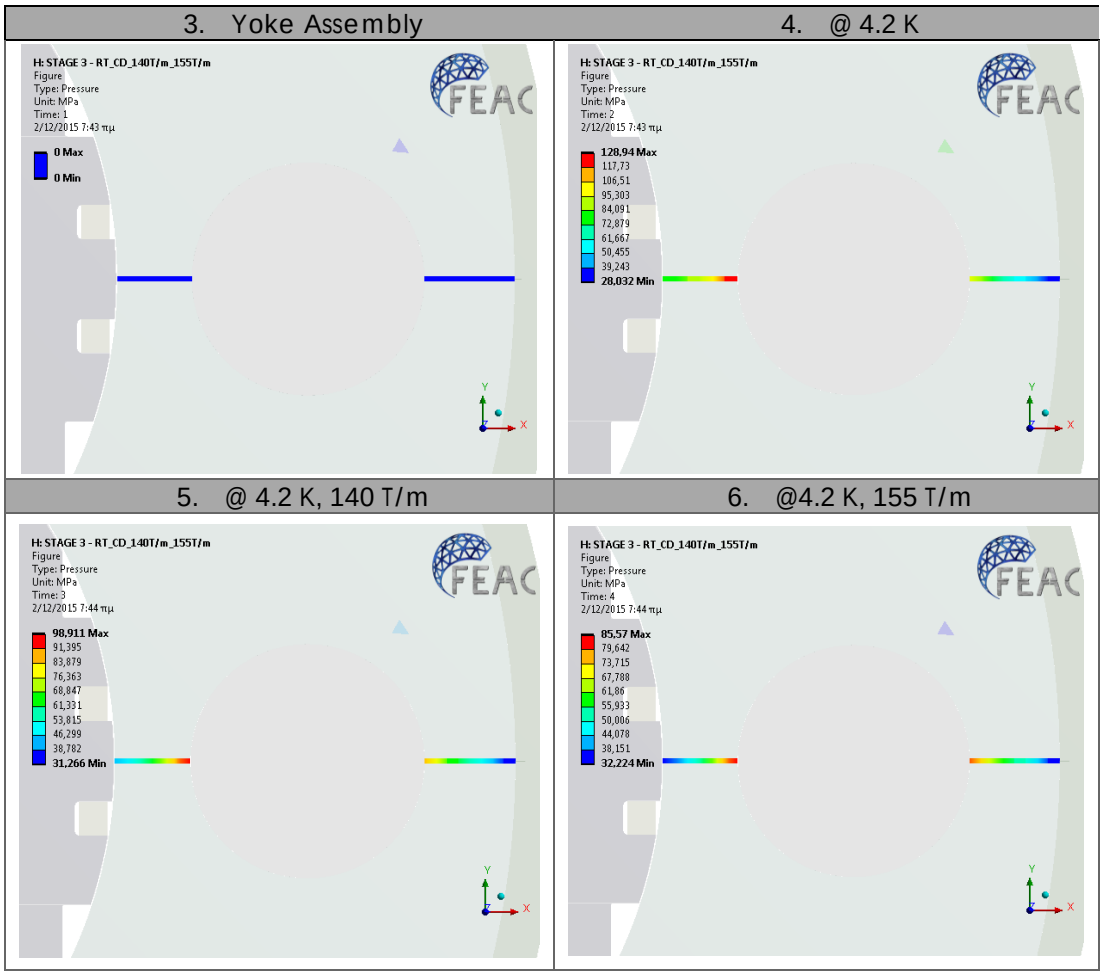

Figure 31: Contact Pressure [MPa] at the yoke mid-plane

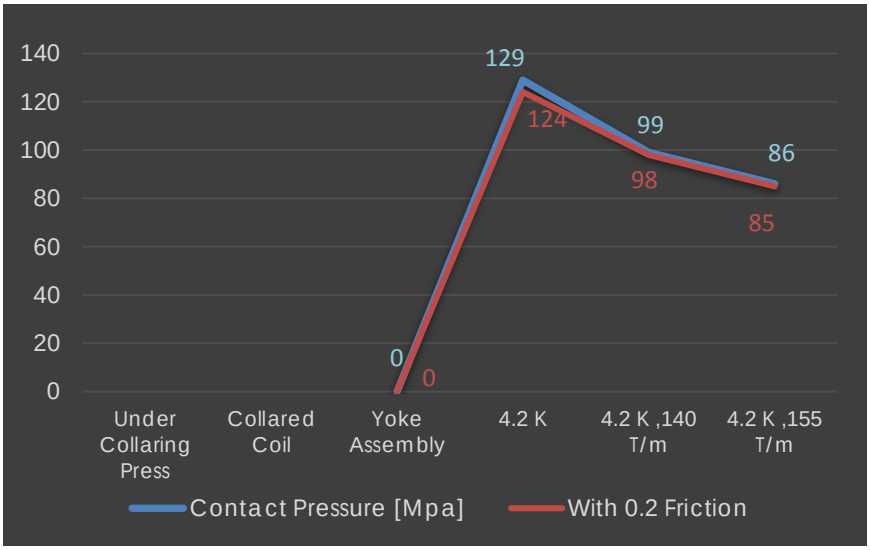

Figure 32: Maximum contact pressure [MPa] evolution in the yoke mid-plane.

5.2.4.6 Al-Bars

The Al-bars control the gap between the two half-yokes at the ambient temperature (Fig. 33 and Fig. 34). On the vertical plane, the contact pressure is slightly lower due to the deformation of the yoke lamination around the collars. The diameter of the Al-bars is chosen to shrink away from the yoke during cool down due to the differential thermal contraction allowing the closure of the yoke gap.

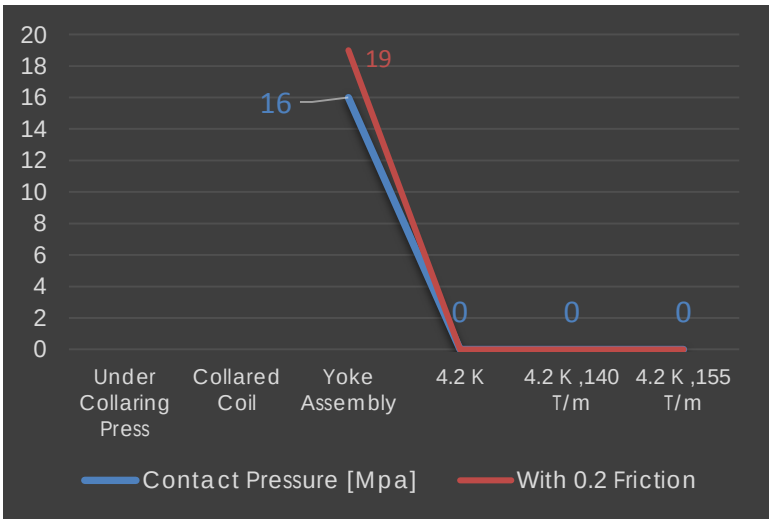

Figure 34: Contact Pressure [MPa] evolution

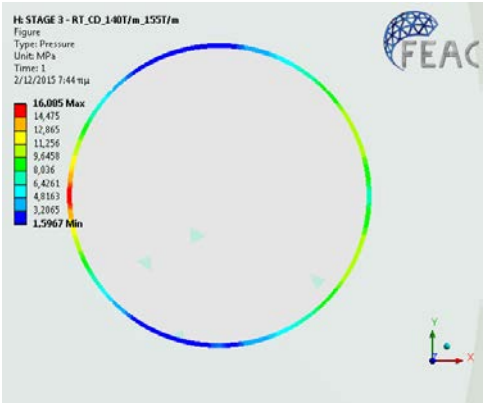

Figure 33: Contact Pressure at the Al-Bars after shell welding

5.2.4.7 Outer Shell

The stainless steel outer shell tension shall remain below 250 MPa at ambient temperature. After the welding process, the peak value of 334 (Fig. 36) MPa is localized in the welding area while the mean stress in the shell remains below 209 MPa as shown in Figure 35.

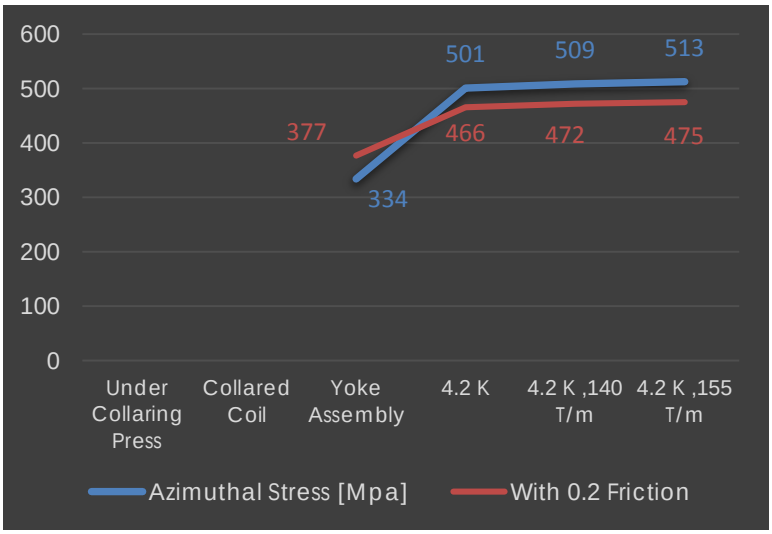

Figure 36: Shell stress [MPa] evolution

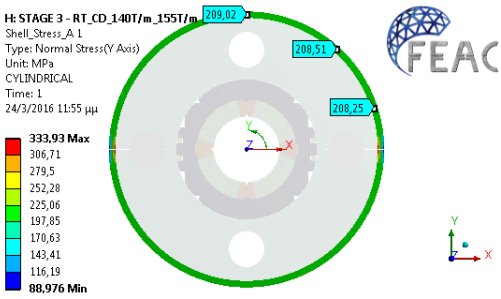

Figure 35: At ambient temperature, 95% of the shell is below 210 MPa

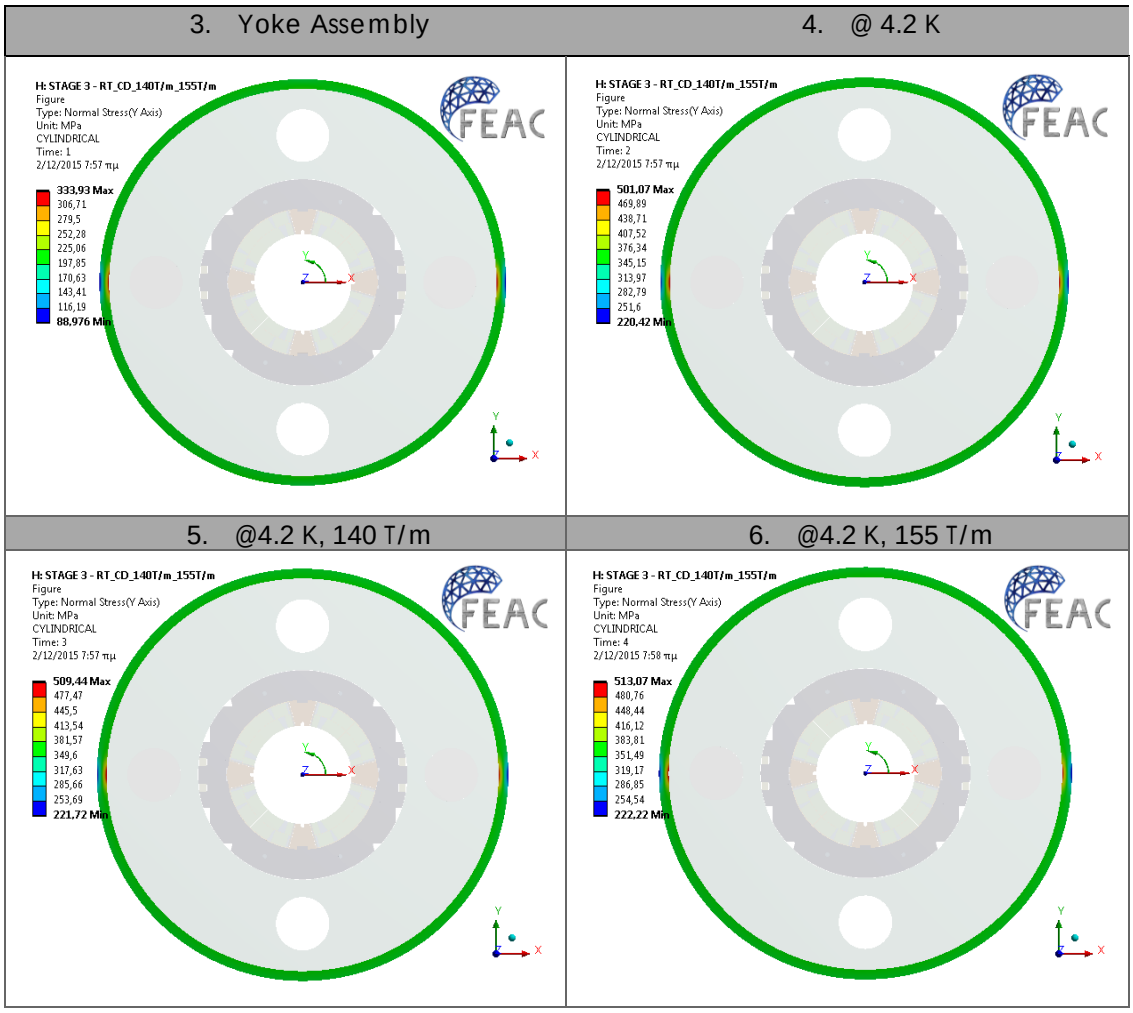

Figure 37: Azimuthal stress [MPa] at all stages

5.3 Magnetic field quality

The deformed shape from the structural analysis was imported in ROXIE to verify the magnetic field quality in the magnet's aperture. The multipoles arising from the mechanical deformation are summarized in Table 3 and confirm the minimal distortion of the quadrupole symmetry along with a very high structural rigidity. The iron saturation, persistent current effects and systematic errors were excluded from the analysis. The systematic offsets of b4 and b6 can easily be suppressed by fine-tuning the coil dimensions and shimming, if required.

	9 T/m	140 T/m	155 T/m
b4	1.6	1.9	1.6
b6	-9.6	-10.3	-10.6
b10	-0.1	0.0	0.0

Table 3: Field Harmonic Components

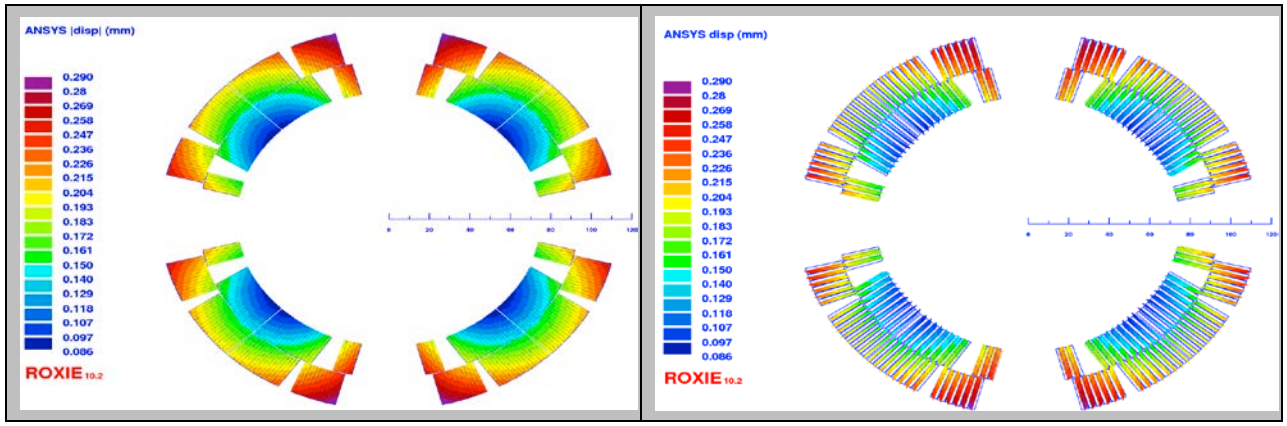

Figure 38: Displacement of conductors [mm] in ROXIE

5.4 Design Space & Sensitivity Analysis

The sensitivity analysis is conducted with the Design Exploration method. This approach uses a deterministic method based on Design of Experiments (DOE). The Design of Experiments (DOE) sets the location of sampling points (finite element evaluations) and a Response Surface is built based on them. In the DOE study the number of the required sampling points is calculated depending on the number of input parameters. Eight input parameters were chosen for this study (Fig. 39), corresponding to 81 sampling points with the CCD (Central Composite Design) method. The produced response surface is a full 2nd-order polynomial. The values of the tolerances used (Table 4), are taken from the 11T Dipole magnet.

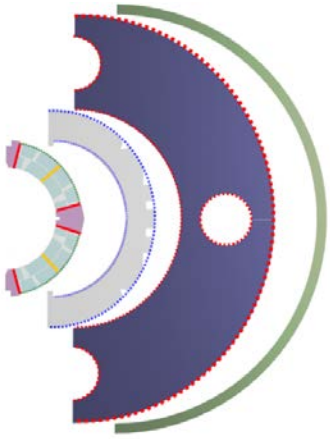

Figure 39: Interfaces included in the DOE

Component	Interface	Tolerance
Yoke	Outer diameter	± 3,8 μm
	Inner diameter	
	Hole's diameter	
Collar	Outer diameter	± 6,3 μm
	Inner diameter	
Coil	Outer diameter	± 75 μm
	Azimuthal length	± 50 μm
Loading plate	Angle	± 0,2°

Table 4: Input parameters for the DOE

Figure 39 shows all combinations amongst the input parameters that have been solved during the DOE step.

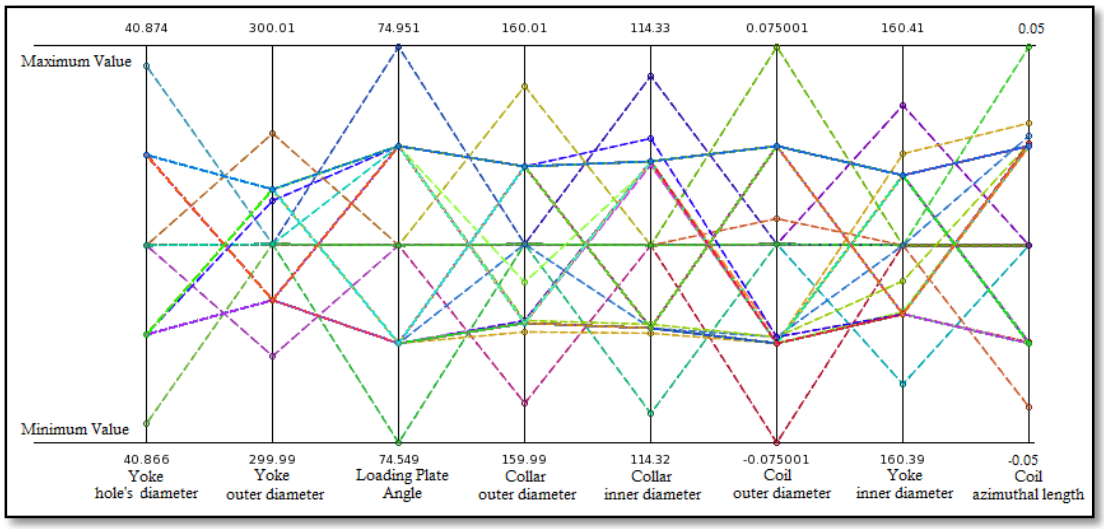

Figure 40: Parameters parallel chart with their minimum & maximum values

5.4.1 Design space for Coil

The design space for the coil is presented in Figure 41. The tolerances at the coil-collar interface and the azimuthal length dominate the peak stress in the coils.

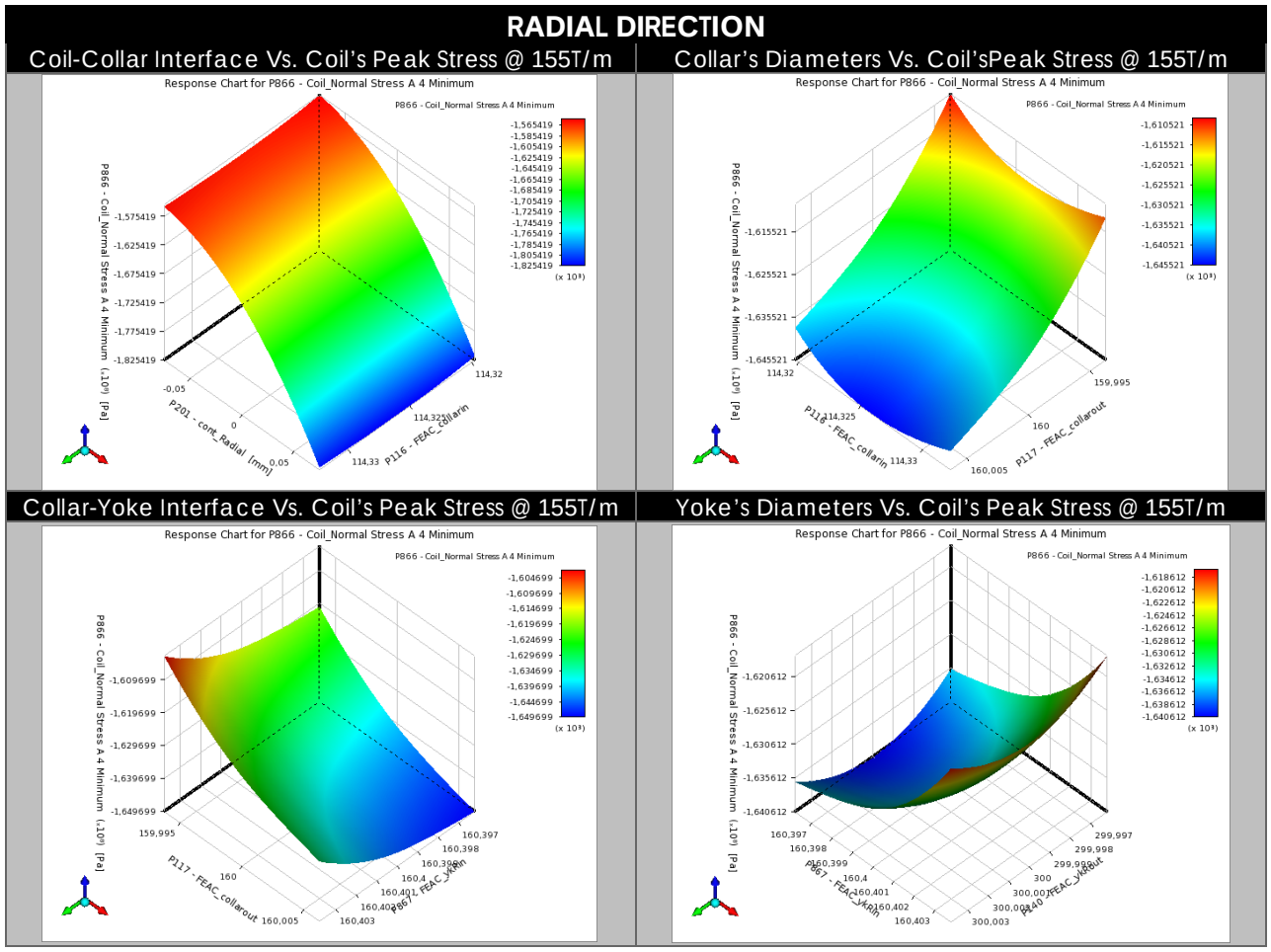

AZIMUTHAL DIRECTION

Loading Plate's Angle & Coil's Azimuthal length Vs. Coil's Peak Stress @ 155T/m

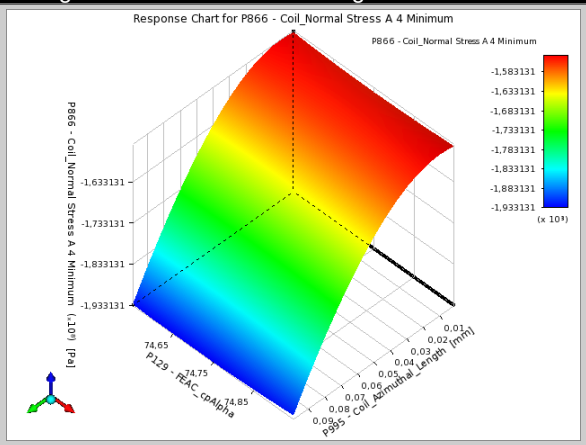

Figure 41: Design space for coil

The sensitivity chart of Figure 42 shows graphically the impact of each input parameter change on the coil peak stress. In the bar chart the negative values correspond to increasing input parameter and decreasing output parameter values. The coil azimuthal size and outer diameter affect more the peak stress than the other parameters. The pie chart shows the same information in a different format.

Sensitivity Chart for Coil's Peak Stress

Bar Chart

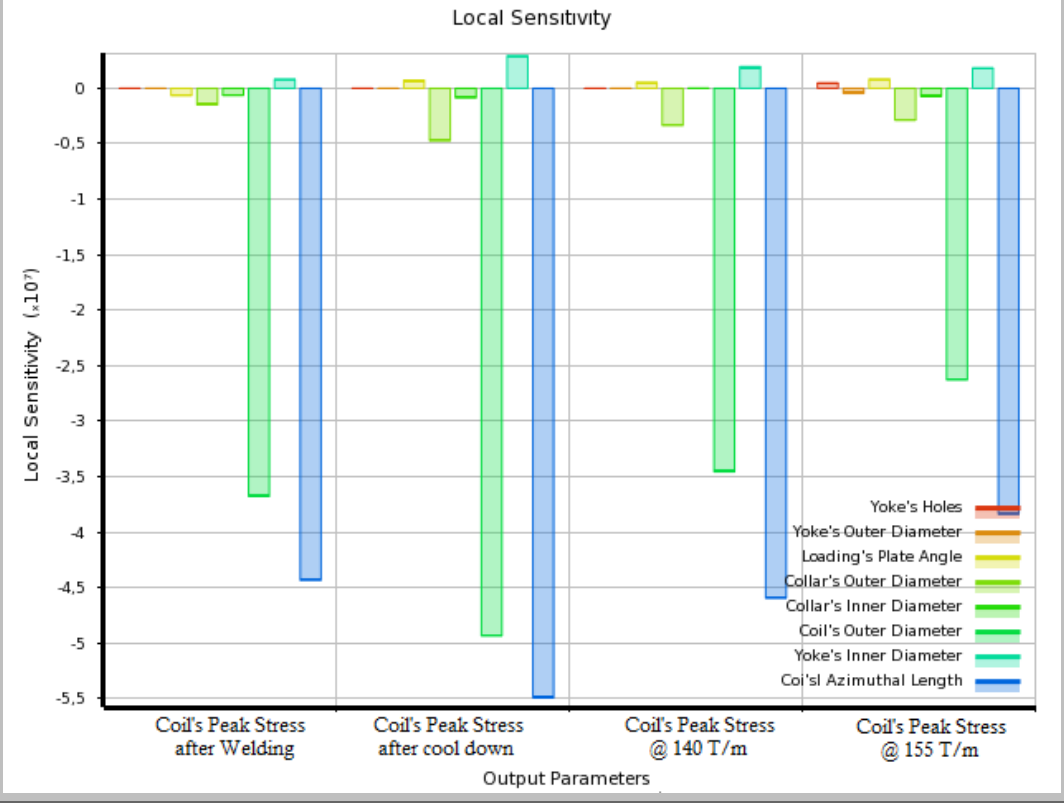

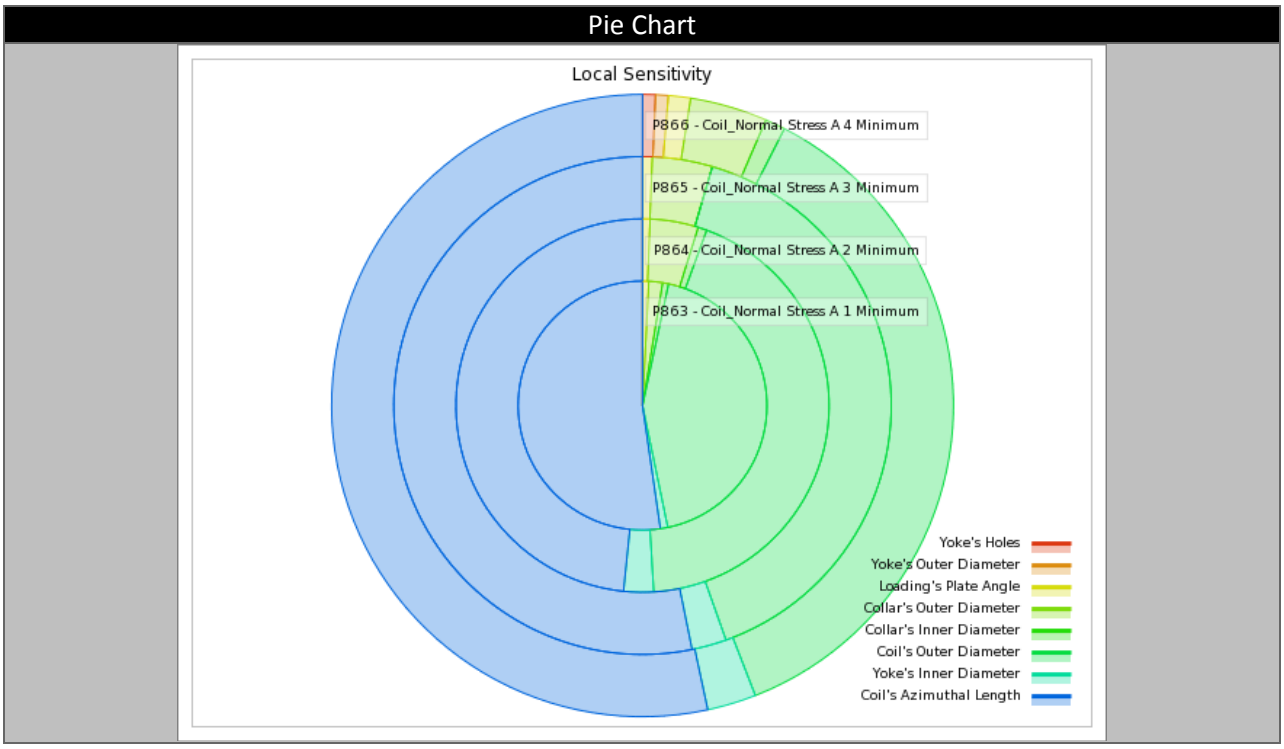

Figure 42: Sensitivity Charts for Coil's peak stress

5.4.2 Contact Pressure

The coil azimuthal size and outer diameter also dominate the Al-bar – yoke and interface between the top and bottom half-yokes as shown in Figure 43.

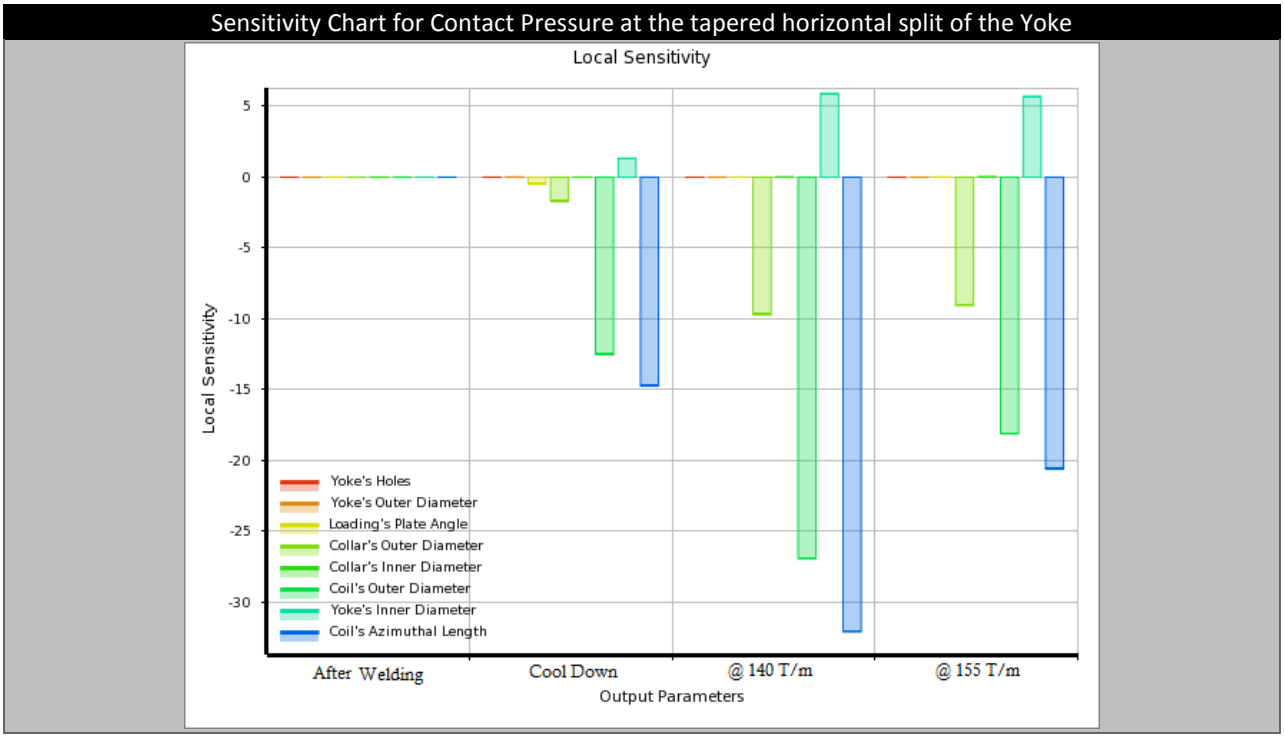

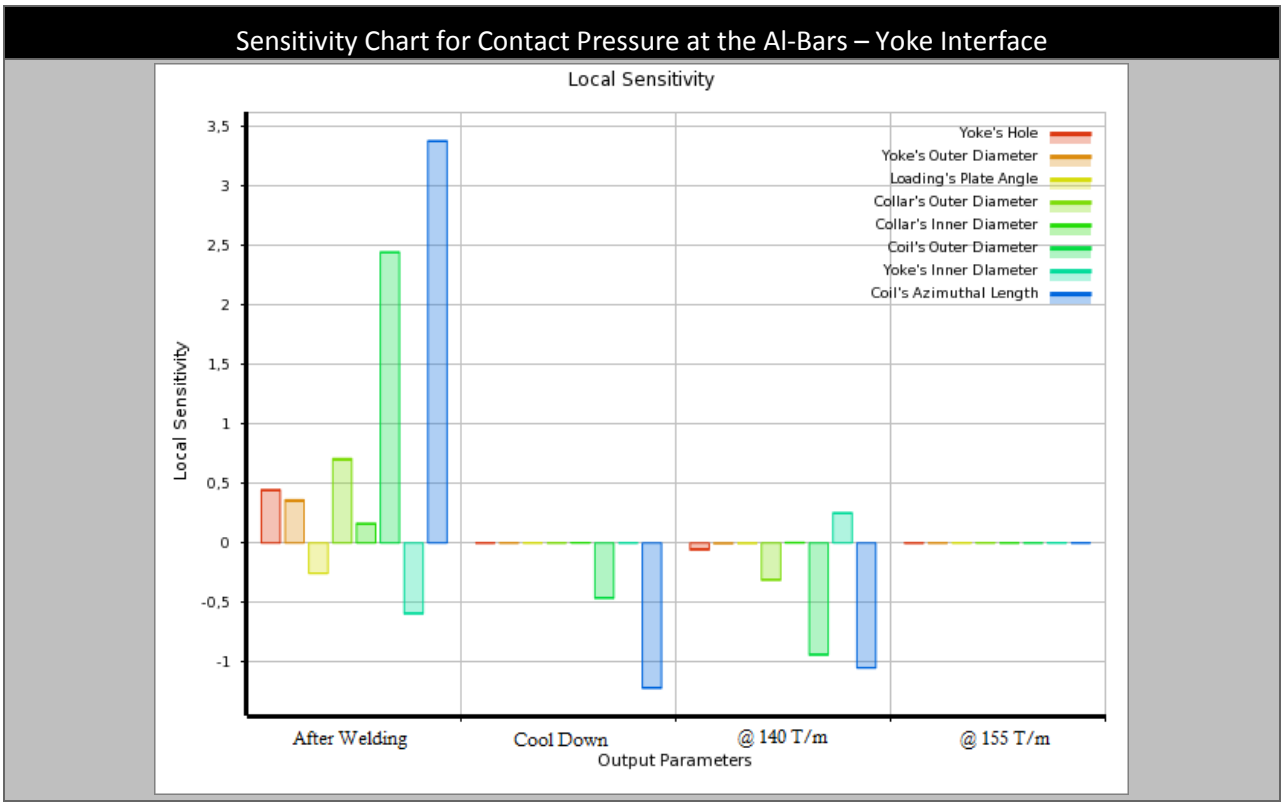

Figure 43: Sensitivity Charts for contact's pressure

6 3D model

The scope of the 3D model (Fig. 44) is to focus at the end region of the magnet and to understand the behavior of the assembly along the longitudinal axis. It is critical to accurately control and minimize the coil's elongation due to the axial magnetic forces.

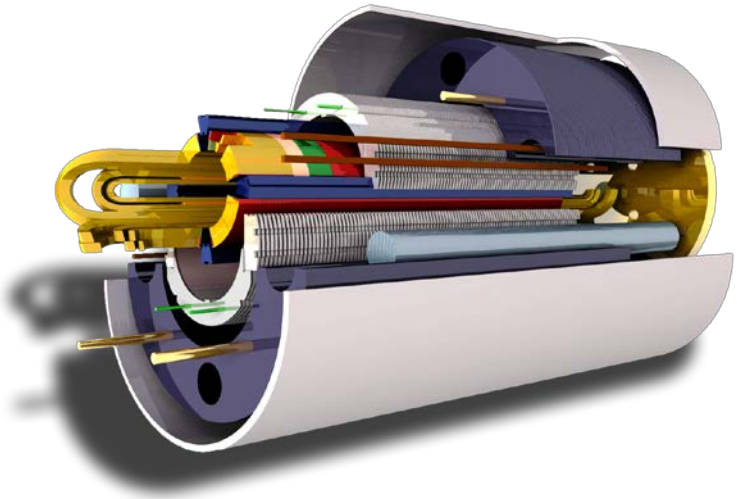

Figure 44: Exploded view of the MKQXF Nb_3Sn quadrupole including the additional longitudinal rods

The design philosophy of the end region is similar to the 11T Dipole (Fig.45). Two rings, one on each side of the magnet, are welded to the end plates of the magnet and the shell. Four tie rods, of 30mm diameter, mounted at 45° degrees, 190 mm from the center of the bore, pass through the yoke laminations and connect the two end plates. The rods decrease the deformation of the end plates, thus reducing the elongation of the coil. Four bullets per end plate provide the option to fine-tune the applied axial pre-stress on the coil. To protect the coil from the bullets and to evenly distribute the applied pre-stress caused by them, a smaller plate is inserted between the coil and the end plate.

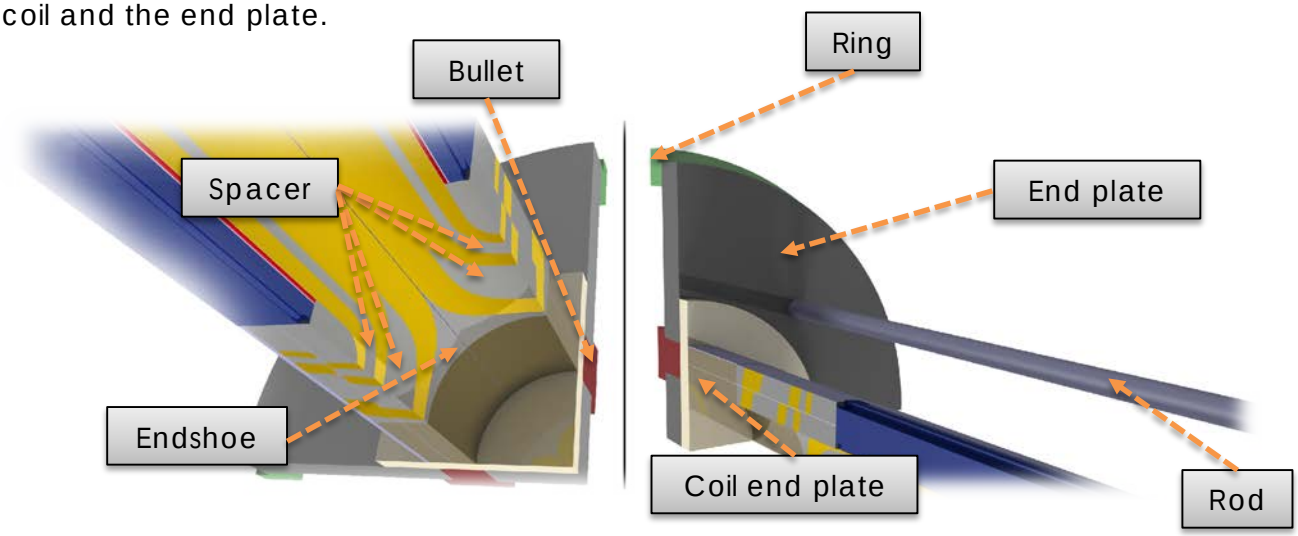

Figure 45: Main components of the end region

6.1 Electromagnetic analysis

The 3D electromagnetic model was analyzed in MAXWELL, to transfer the electromagnetic forces to the structural analysis model. The distribution and magnitude of the magnetic field was in very good agreement with ROXIE results (Table 5). The mesh on the conductors is very dense and a non-linear BH-curve was used to describe the magnetization of the yoke.

Gradient T/m	Peak magnetic field (T)		Fz (MN) per magnet	
	ROXIE	MAXWELL	ROXIE	MAXWELL
132.6	11.19	11.18	1.20	1.17
140	11.81	11.82	1.31	1.30
155	13.09	13.16	1.76	1.72

Table 5: Comparison of the peak magnetic field & the axial forces between ROXIE and Maxwell

The magnetic field at 140 T/m & 155 T/m is shown in Figure 46 and 47.

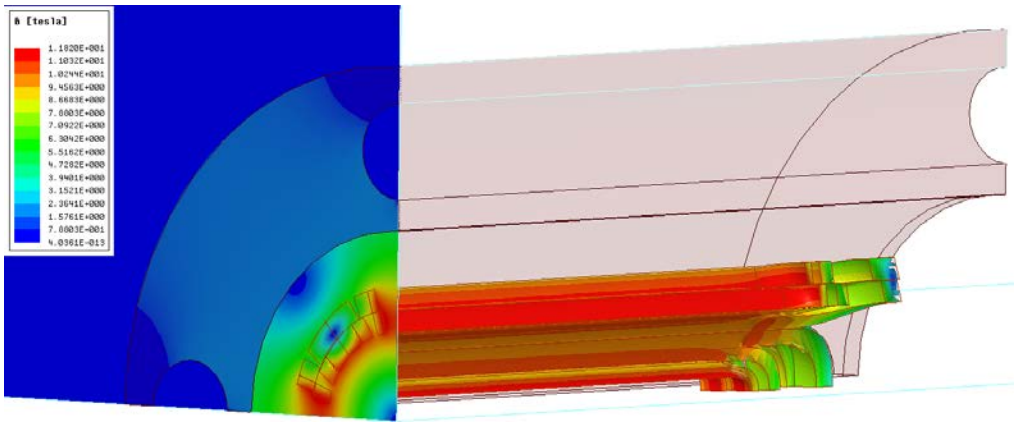

Figure 46: 11.82 T, 140 T/m

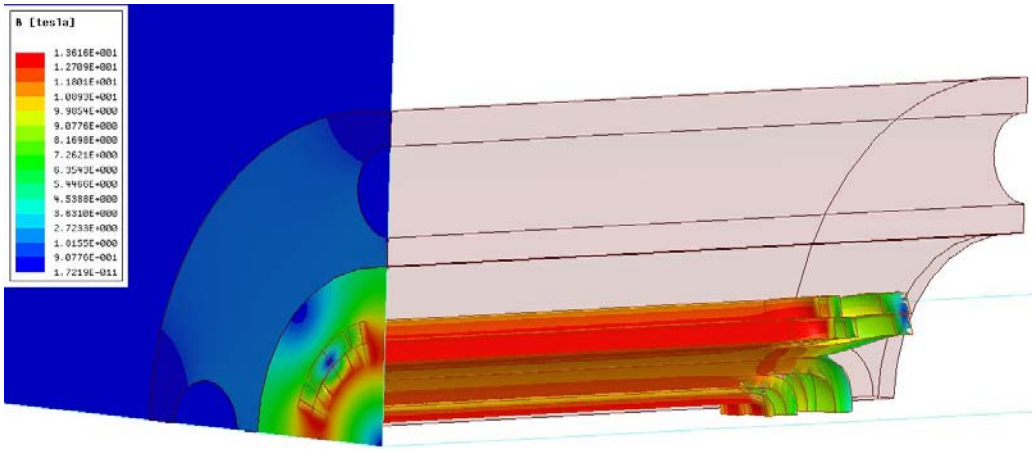

Figure 47: 13.16 T, 155 T/m

The electromagnetic forces were transferred using the ANSYS Workbench environment and all nodes from the MAXWELL model were mapped on the structural mesh (Fig. 48).

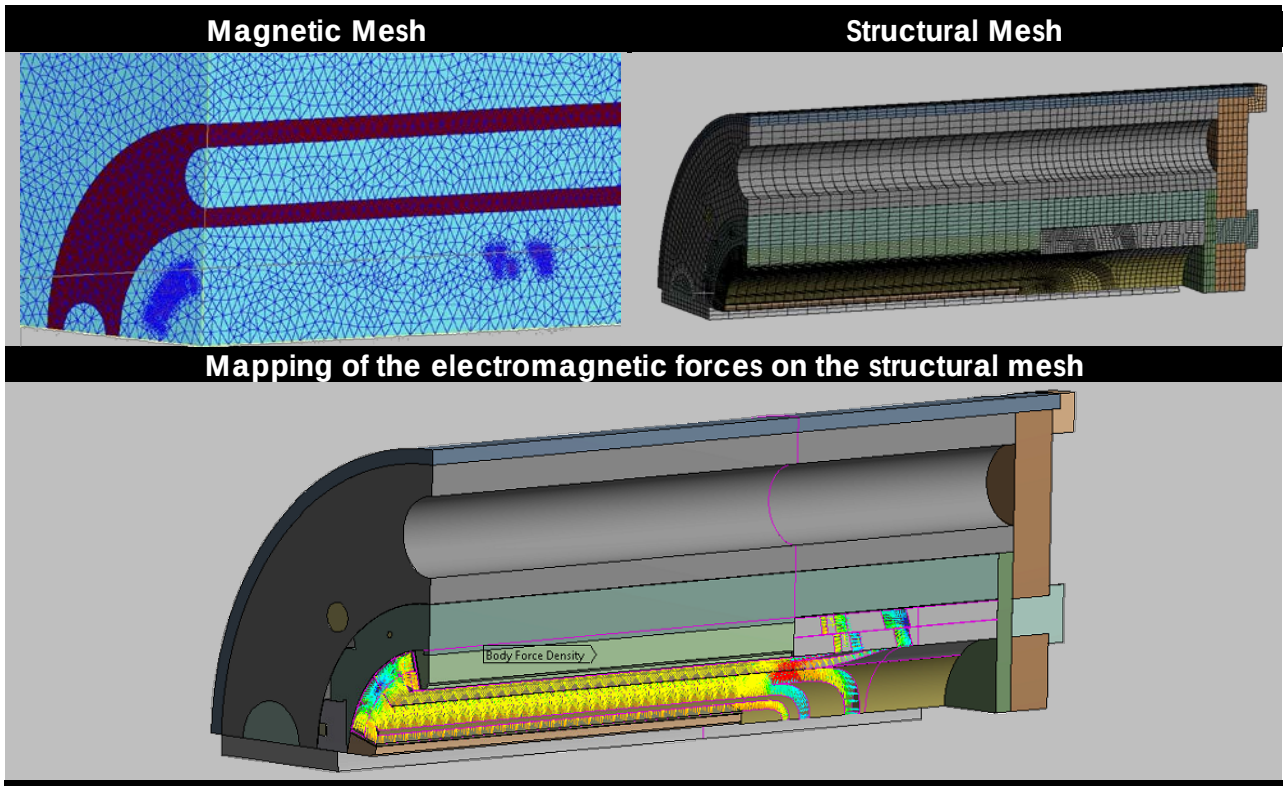

Figure 48: Mapping of the electromagnetic forces on the structural mesh

6.2 Structural analysis

6.2.1 Finite Element model

The ANSYS® Workbench project schematic was further enriched with the addition of the 3D analysis systems, as shown below (Figure 49).

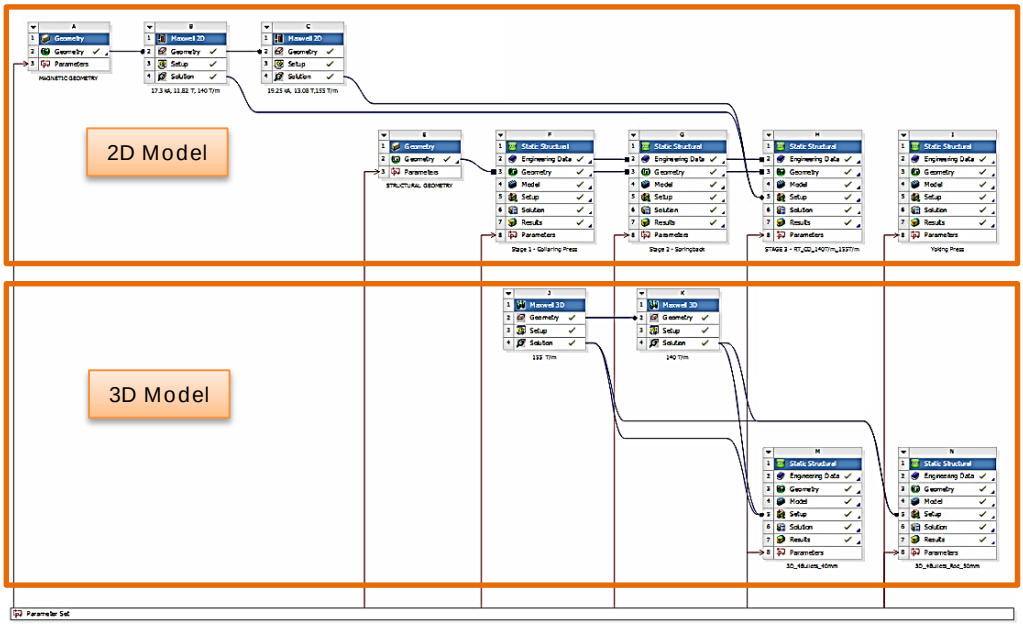

Figure 49: the ANSYS Workbench environment, including both the 2D & 3D analysis

To reduce the computational cost of the model, only one-eighth of the geometry was used and 3 symmetry planes were defined. Similar to the 2D Model, the coil block comprising the windings, the wedges, the interlayer insulation, the spacers, the end shoes and the trace was modeled as a multi-body part. Hence, no contacts were required since all nodes were merged. The conductor was meshed with high quality swept hexahedral elements while the remaining elements of the coil block were hex dominant. All other parts were meshed with swept, hexahedral elements (Fig. 50).

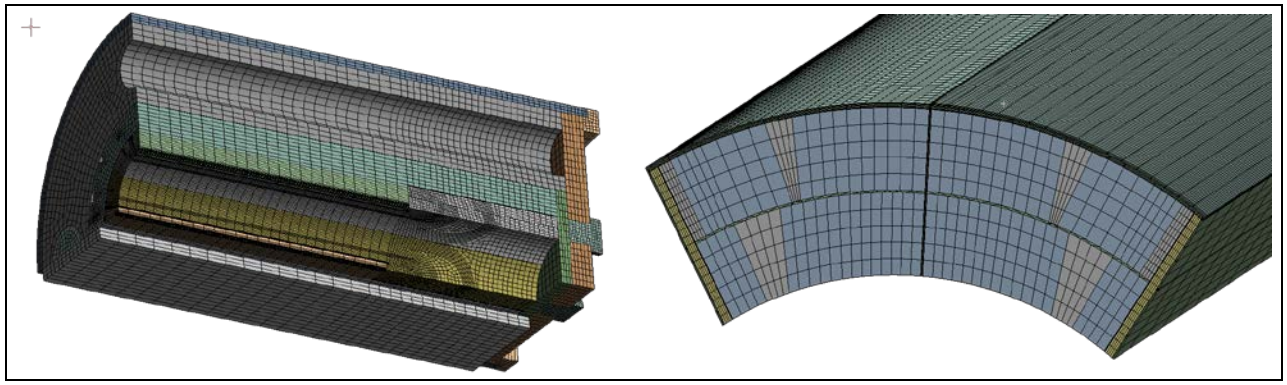

Figure 50: Structural mesh

The short/long collars and the yoke were not modeled as multi-layered parts. They were merged instead as this simplification hardly affects the behavior of the magnet ends that was under study. Consequently, the contact type definition at the keys-collars and short-long collars interface was changed to bonded. Compared to the 2D analysis, some additional contacts were introduced to describe the behavior between the parts along the longitudinal axis. The model was frictionless.

Two additional pieces were introduced in the 3D model. In the horizontal plane, a piece was used to simulate the contact between the tapered half yokes. A filler piece was introduced between the coil and the collars, in the extension of the horizontal pole wedge towards the end plate (Fig. 51).

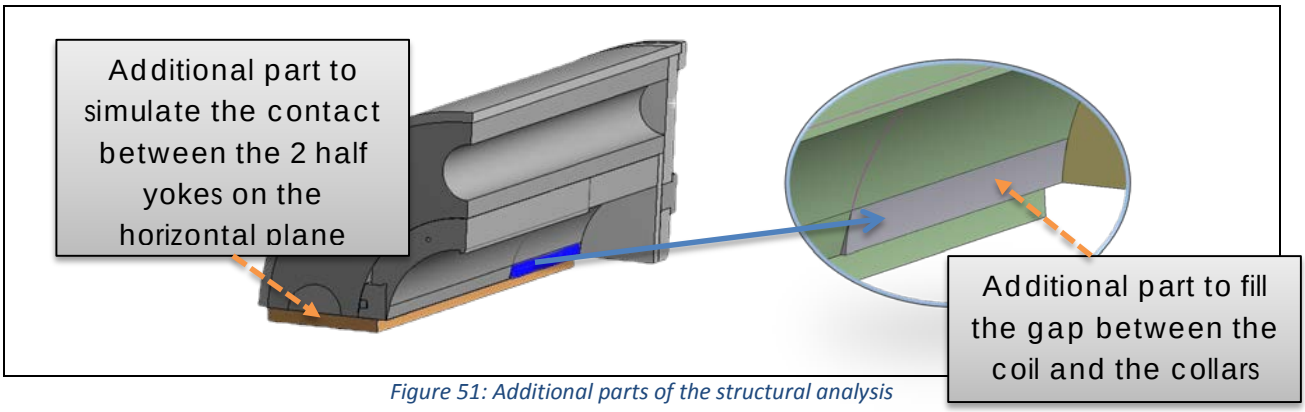

Figure 51: Additional parts of the structural analysis

The symmetric structural model has a length of 775mm although the demonstrator magnet is 2m long. The E-modulus of the st. steel rod that connects the two end plates of the magnet was scaled down, to accurately model the behavior of the assembly

over the total length of the magnet. The applied pre-stress at the bullets-coil's end plate interface was applied through gap elements. The rest of the assembly parameters were identical to in the 2D model. The carefully determined contact definitions and the very good quality of the finite elements ensured a fast convergence of the model.

6.2.2 Load Cases

Four (4) load-steps were considered in the 3D Finite Element Analysis (FEA):

1. Yoke assembly at 293 K.
2. At 4.2 K.
3. At 4.2 K, 140 T/m.
4. At 4.2 K, 155 T/m

6.2.3 Results

6.2.3.1 Total displacement of whole structure

Figure 52 gives an overview of the total displacement of the magnet. During the yoke assembly, the shell is vertically displaced to simulate the welding process, while the bullets provide the necessary pre-stress to the coil. The cool down to 4.2 K of the magnet follows afterwards. While at 4.2 K, the magnet is powered on and the structure counteracts the Lorentz forces of 1.3 & 1.72 MN (Table 5).

1. **Yoke Assembly**	2. **@ 4.2 K**
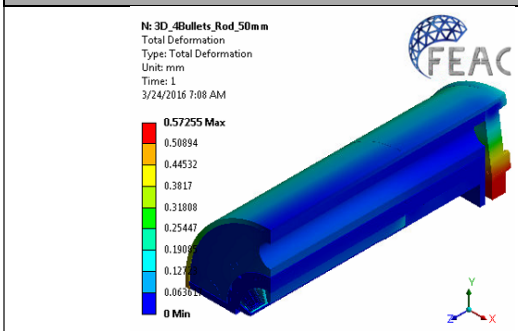	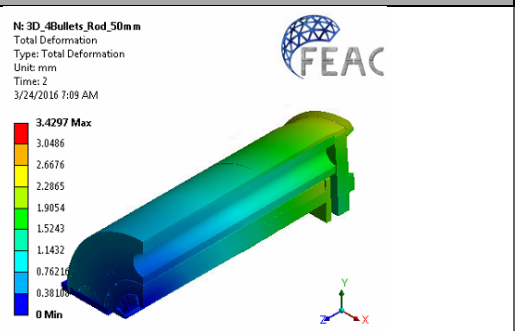
3. **@ 4.2 K, 140 T/m**	4. @4.2 K, 155 T/m
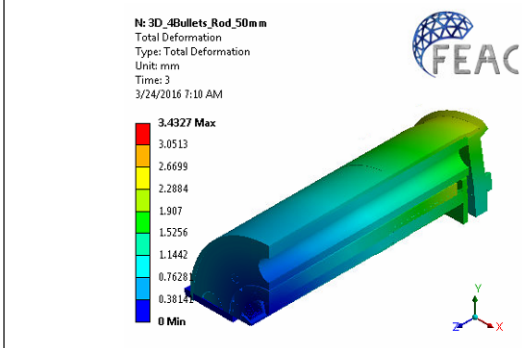	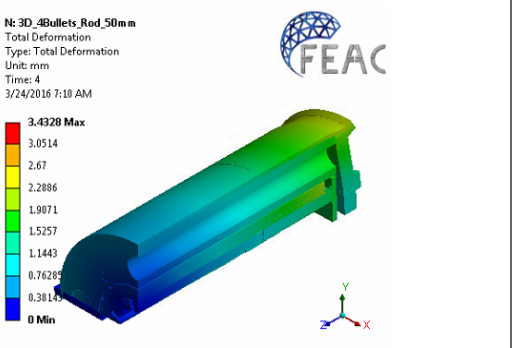

Figure 52: Total displacement of magnet [mm], scale x50

6.2.3.2 Longitudinal deformation of coil for several scenarios

An excessive deformation of the coil block might cause irreversible degradation of the conductor. Consequently, it is crucial to keep its longitudinal elongation within the safe limits. Typically, the elongation of the conductor shall be kept below 0.3% of its total length ($u_z < 0.3\% * L_{coil}$). The safe limits can be seen below (Table 6):

Magnet	Length [m]	Maximum allowed elongation 0.3%
FEA model	1.55 m	4.65 mm
Demonstrator magnet	2 m	6 mm
Full length magnet	5.5 m	16.5 mm

Table 6: Maximum allowed elongation

Several scenarios were studied during the optimisation including three main parameters: (i) the end plate's thickness (ii) the introduced gap, which simulates the applied pre-load by the bullets, in the bullets-coil end plate interface and (iii) the addition of the ø30 mm rod.

Finally, a thickness of 50 mm was chosen for the end plate, with the addition of the tie rods and 0.5 mm gap elements. The structure provides a possibility to increase the axial coil pre-load by further tightening the bullets (2mm gap elements, Fig. 53).

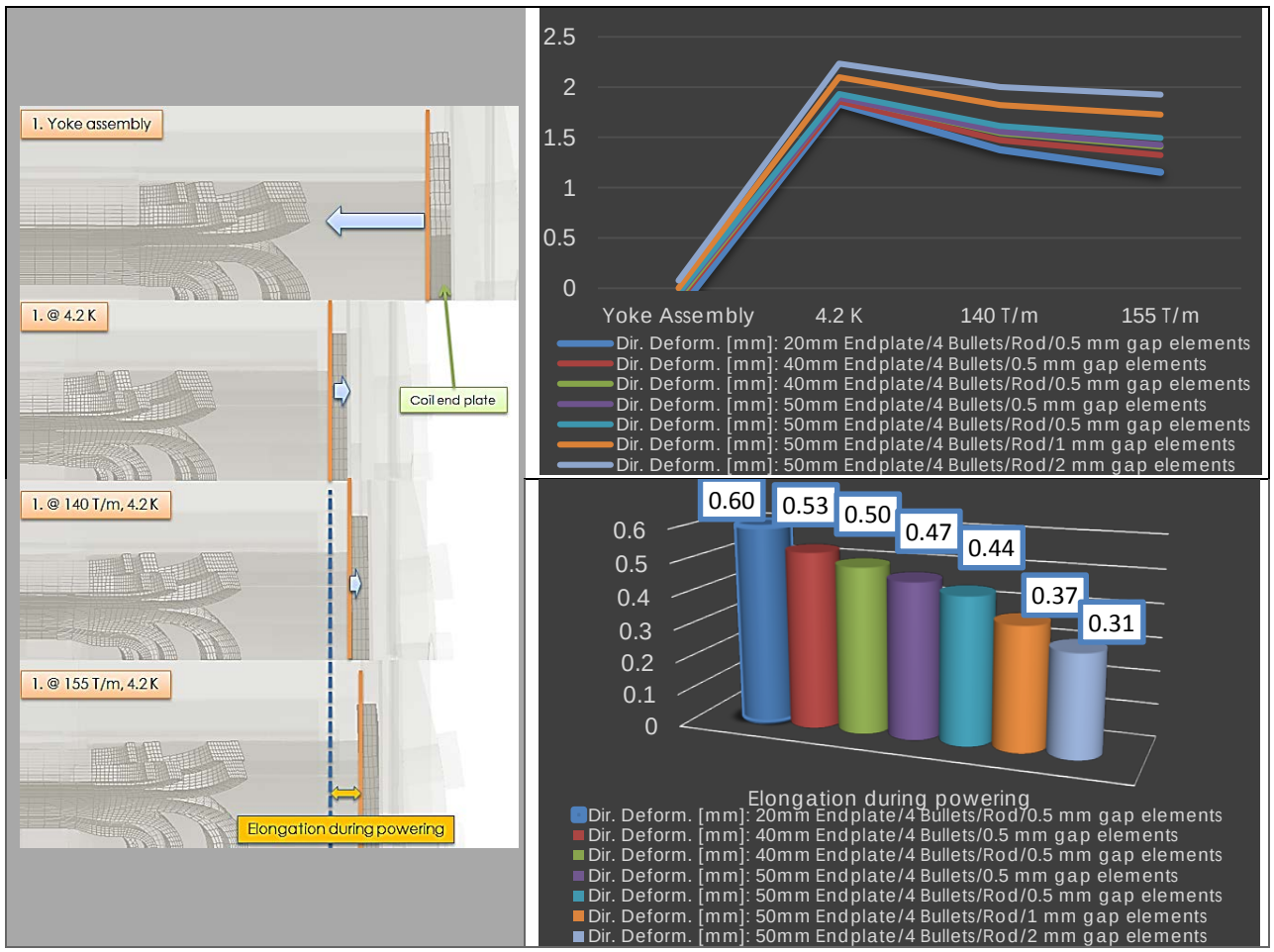

Figure 53: Longitudinal deformation of coil ends [mm]

6.2.3.3 Model with 4 Bullets, 50 mm End plate, Rods & 0.5 mm gap elements

6.2.3.3.1 Directional deformation of coil & end plate

The directional deformation of the end plates and the coil's extremities is presented in Figures 54 & 55. The effect of the pre-loading due to the bullets can be clearly seen in red color on the horizontal and vertical axis. The deformation is very symmetric across the cross-section at all stages.

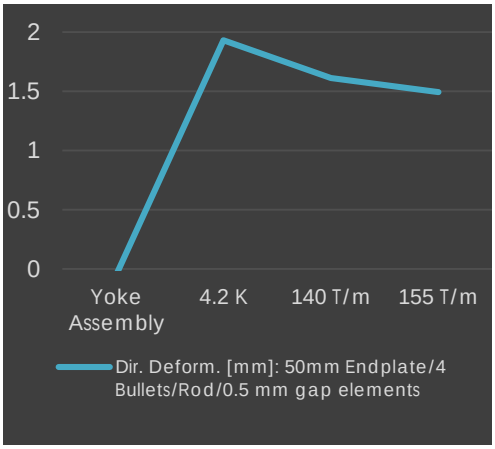

Figure 54: Elongation of coil's extremities [mm]

At the yoke assembly stage, the end plate deforms due to the tightening of the bullets. The bullets push against the coil, which at the same time is elongated due to the poisson effect by the pre-stress applied at the poles through the horizontal and vertical shims. During cooling down, the coil shrinks more than the system of the rods with the end plates and the bullets. At 140 T/m and 155 T/m this system provides a rigid longitudinal envelope allowing the coil to only elongate by 0.44 mm from its initial position at 4.2 K.

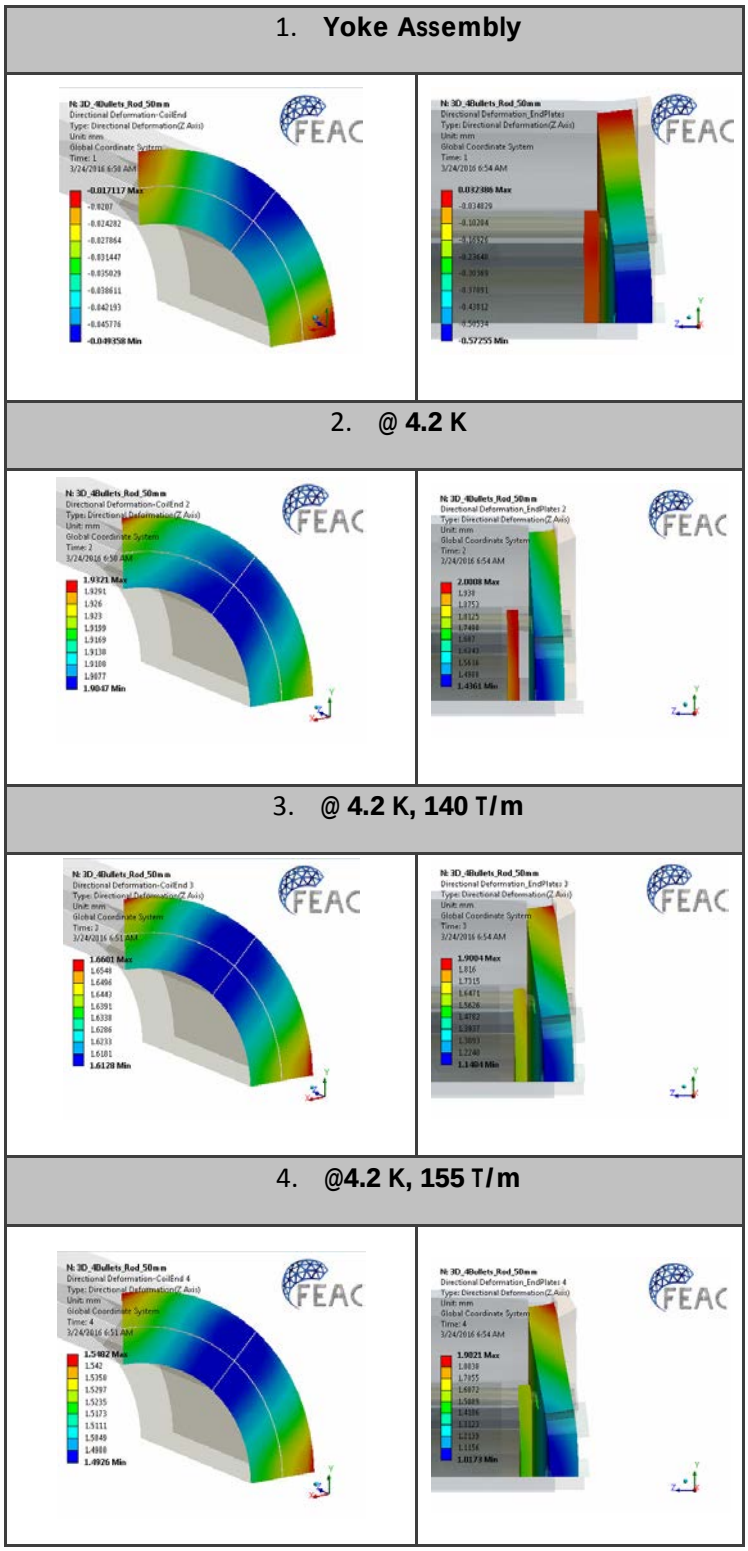

Figure 55: Directional deformation of coil and end plate [mm], scale x50

6.2.3.3.2 Coil stress

The 3D model replicates very well the stress field distribution of the 2D model, in any xy-plane along the straight section. At 140 T/m & 155 T/m the very rigid structure keeps the stress distribution uniform. At the coil mid-plane, the maximum stress on the inner layer ranges from -143 at 140 T/m to -166 MPa at 155 T/m (Fig. 56).

Focusing at the 3D coil and not just at a cross-section, the peak stress is located, as expected, across the transition zone from straight to the end region (Fig. 44). This is explained by the fact that some parts, which are described in chapter 3.2 (Coil design) and illustrated in Fig. 5 (e.g. first end spacer, short pole wedge), had to be simplified which made the transition zone more rigid.

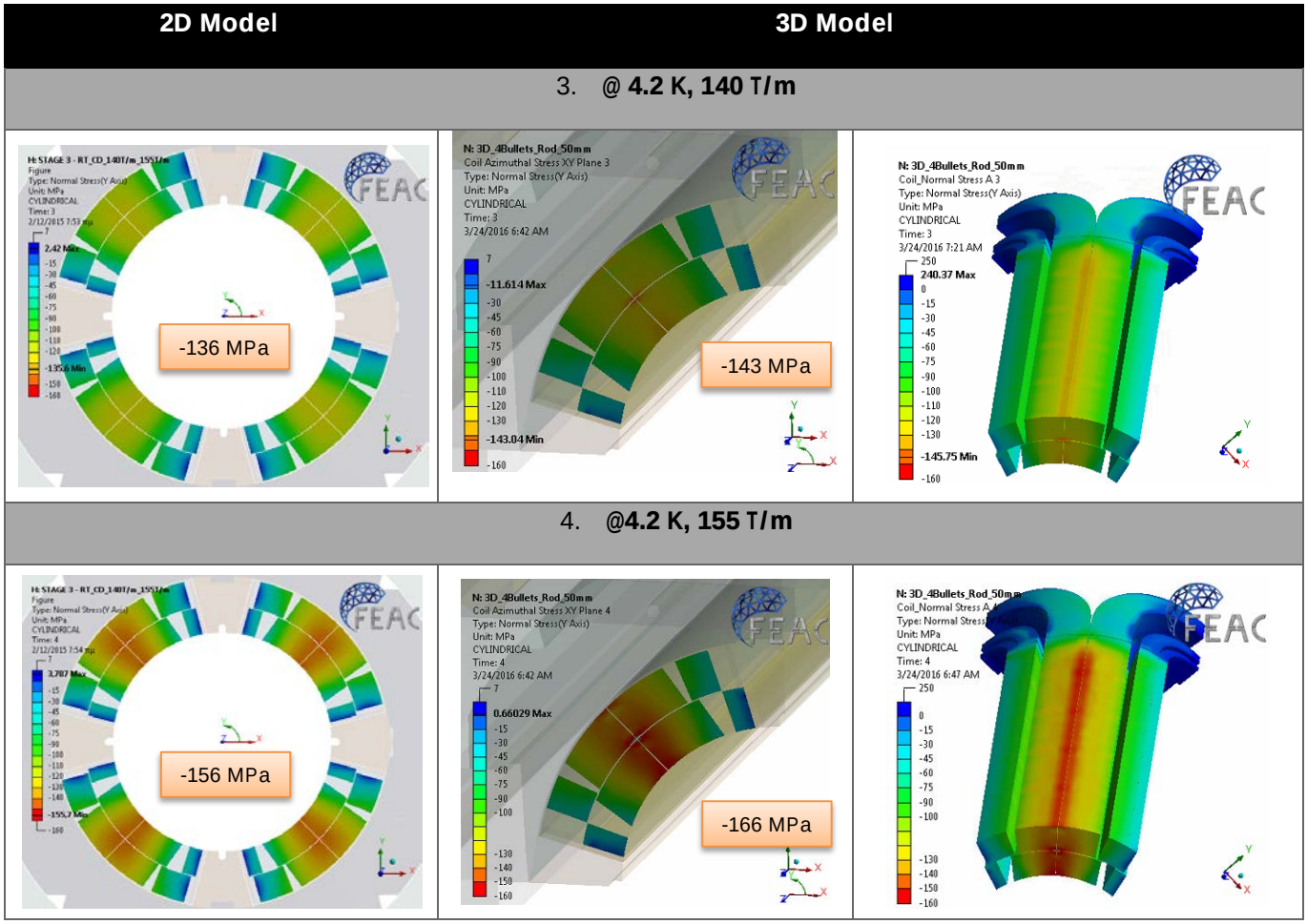

Figure 56: Azimuthal coil stress [MPa] and comparison with the 2D results

6.2.3.3.3 Coil's radial deformation

The design goal is to achieve a symmetric deformation of the vertical and the horizontal pole turns during cool down, to prevent any distortions from quadrupole symmetry. Figure 57 shows the radial deformation of the coil and provides a comparison between the 2D & 3D model results. The trend of the deformation is similar in the 2D & 3D model. During cooling down the yoke gap is firmly closed restoring the

circular symmetry of the coil assembly. At 4.2 K, there is a difference of 0.08 mm between the 2D and the 3D model which can be explained by the simplifications applied in the 3D model and the presence of the magnet's end regions.

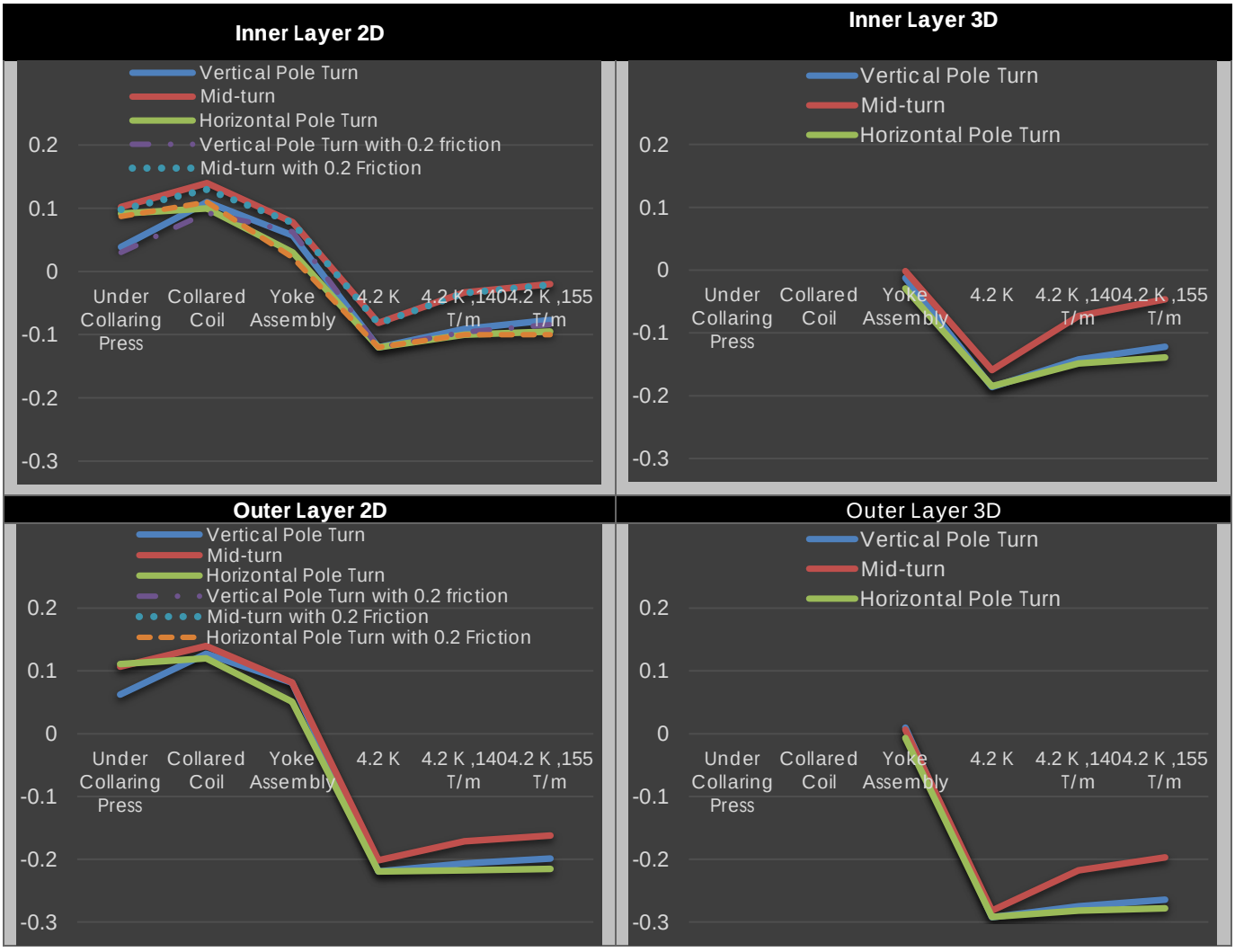

Figure 57: Radial Deformation of coil [mm] and comparison with the 2D results

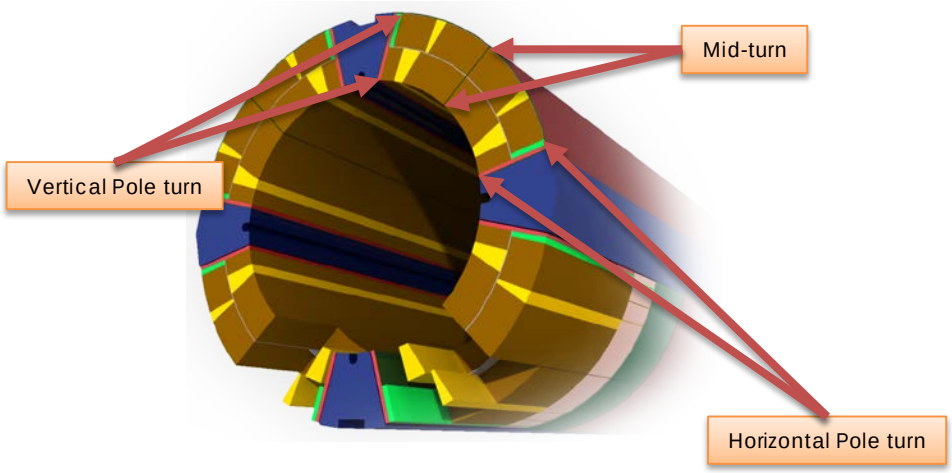

6.2.3.3.4 Collar's radial deformation

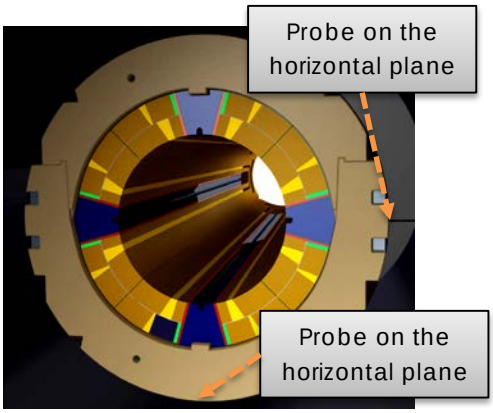

The evolution of the radial displacement of the collar outer radius along the horizontal and vertical axis relative to the nominal (free) dimensions is shown in Figure 58. After cool-down the circular symmetry is restored. During powering the horizontal split yoke provides somewhat less support for the coils and some horizontal deformation can be observed, whereas in the vertical plane such deformation is not present up to 155 T/m. The correlation between the 2D & 3D results is very good, showing identical behavior of the structure.

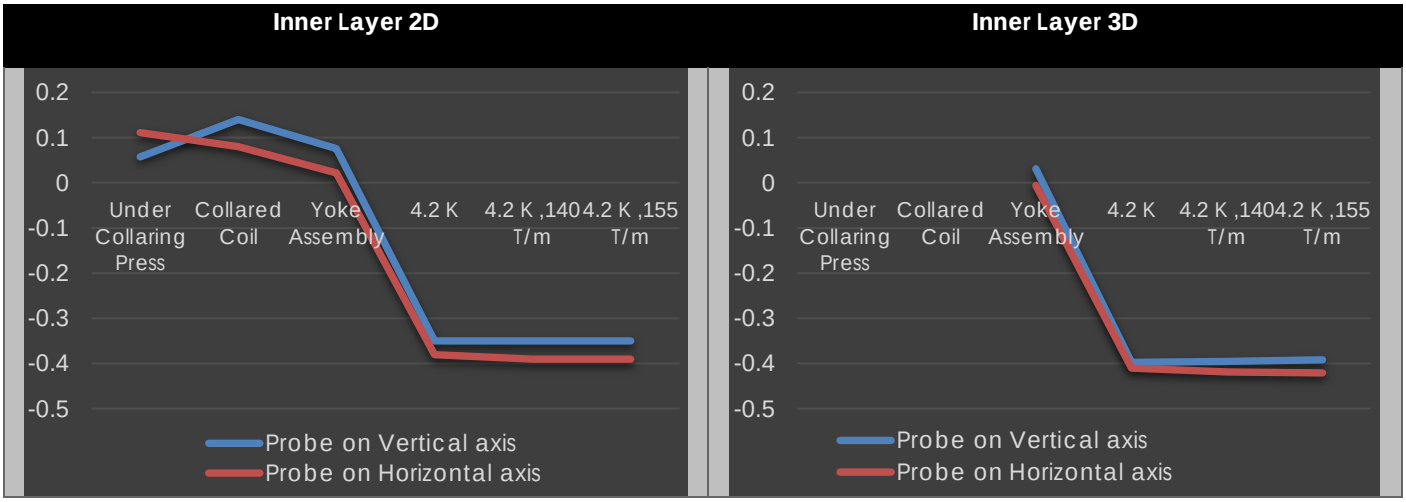

Figure 58: Collar radial deformation [mm] and comparison with the 2D results

6.2.3.3.5 Shell stress

The stainless steel outer shell tension shall remain below 250 MPa at ambient temperature. After the welding process, the peak value is localized in the welding area while the mean stress in the shell remains below 225 MPa. The 3D model results for the straight part of the shell correlate very well to the 2D results (Fig 60). In the end region of the magnet, the deformation of the endplate increases locally the stress field (Fig.59).

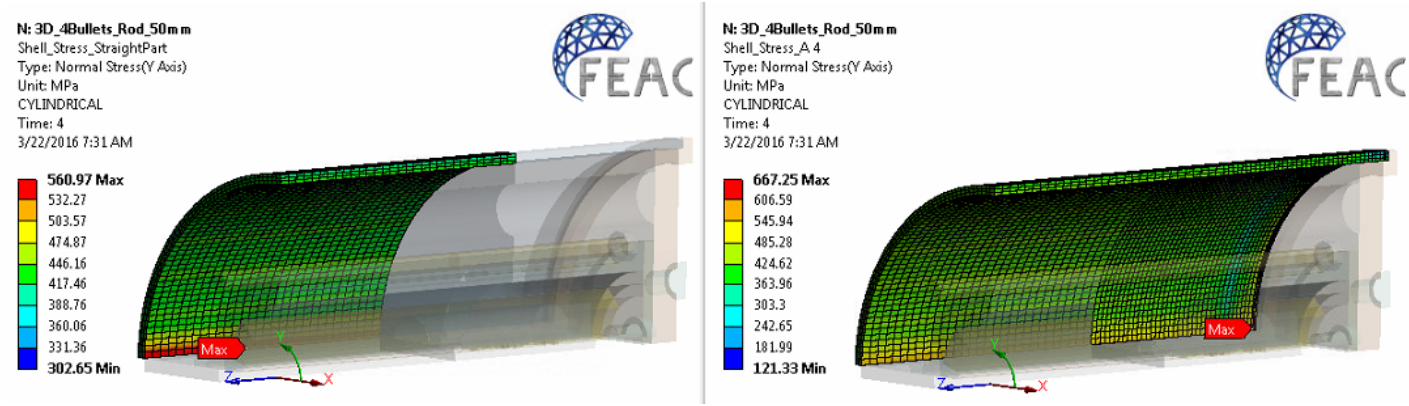

Figure 59: Azimuthal stress [MPa] at 155 T/m, in the straight section of the model (left) and including the end region (right)

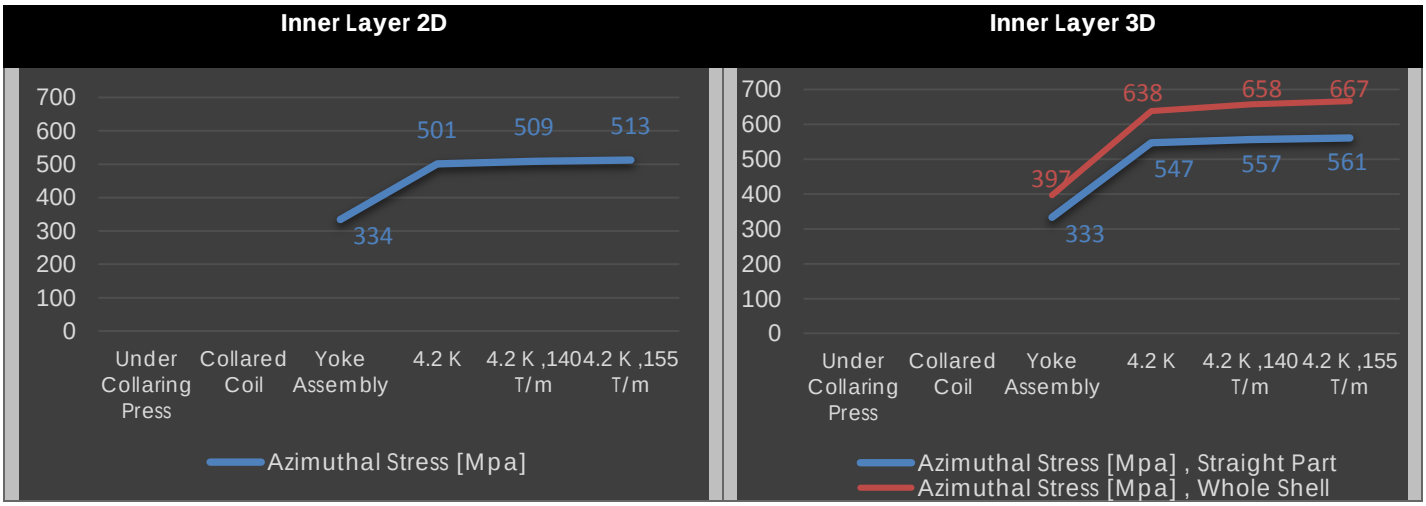

Figure 60: Shell azimuthal stress [MPa] and comparison with the 2D results

6.2.3.3.6 Yoke stress

Similar to the 2D model, the general rigidity of the yoke laminations, which in the 3D model have been assumed as a solid part, is reduced by the heat exchanger holes and the horizontal split plane (Fig. 61). As described in section 5.2.4.5, during the yoke assembly the interference between the collared coil and the yoke around the vertical axis induce slight bending of the yoke lamination around the collared coil. To compensate for this and to store the strain energy in the yoke, the mid-plane has a slight taper. Along the horizontal plane the contact pressure at the collar-yoke interface is enough to bend the region between the heat exchanger hole that locates the Al-bar and the collared coil. The correlation between the 2D & 3D results is shown in Figure 62.

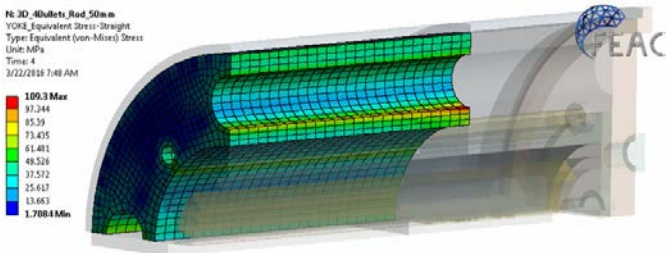

Figure 61: Yoke Stress [MPa] at the straight section

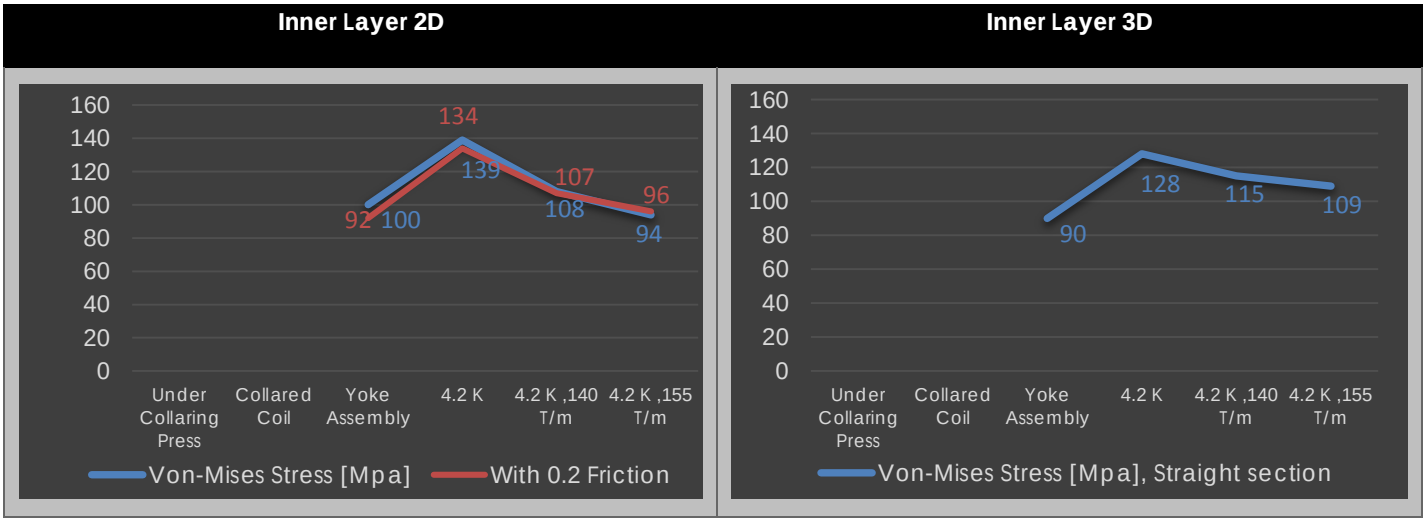

Figure 62: Yoke stress [MPa] and comparison with the 2D results

7 Conclusions

A detailed structural optimization of the new Nb_3Sn quadrupole design concept based on pole-loading and dipole-type collars has been carried out using fully parametric multi-physics FE-model and advanced CAD tools. To make a maximum use of existing coil fabrication tooling and infrastructure the demonstrator magnet design is based on the HL-LHC QXF coils that can be used as-is with minor modifications in the fabrication process.

The FEA shows that coil pre-stress can be applied in a well-controlled manner during the collaring and easily tuneable shimming allows the compensation of coil dimensional variations and mechanical tolerances of the magnet components. To counteract the very large electro-magnetic forces the pole-loading concept provides the "tuning knobs" to tailor the coil pre-stress such that it is the highest at the pole and the lowest at the coil mid-plane at 0-current. The tapered-shape of the mid-plane poles together with the dipole-type collars makes it possible to carry out the collaring process in a dipole-type press and simultaneously over the entire coil length. The very rigid collars minimise the elliptic deformation after the collaring.

The horizontally split iron yoke with a closed gap at operating temperature up to the ultimate design gradient of 155 T/m provides a very rigid structure around the coils minimizing any conductor movements and distortions from the ideal coil geometry. The Al-bars control the yoke gap during the assembly phase and limit the stress level in the coils. The stainless steel shell assembly parameters are achievable and the stresses remain at an acceptable level at all times.

The sensitivity analysis shows that the tolerances used in the study, originating from the 11 T dipole experience, create a design space, which is within the acceptable limits for all components. As expected, the dimensional tolerances on the coil size play the most important role on the maximum coil stress level, underlining the need for high precision metrology of the coils to carefully determine the assembly parameters. During the model magnet phase the shims can easily be adjusted to generate the required pre-stress levels and to compensate for the field errors. These data can then be used at a later stage to adjust the coil fabrication tooling to meet both mechanical and magnetic requirements.

The mechanical design of the end region, including four tie rods, four bullets per side and a 50mm thick end plate, provides the necessary rigidity to the structure and minimizes effectively the elongation of the coil. The 3d model confirms the 2D results and the overall behavior of the structure.

A short demonstrator magnet could be constructed and tested with a very moderate investment in magnet components using the existing QXF coil geometry. The main advantage would be that all existing coil fabrication tooling could be used as such profiting from the QXF conductor and coil development. The parametric CATIA models created as part of this design optimization together with the sensitivity analysis allow very rapid production of the manufacturing drawings of the missing magnet

components including the collars, yoke laminations, pole wedges, and the outer shells.

This collared quadrupole concept can easily be extended to any length, and also applied on a 2-in-1 configuration, which opens very interesting prospects for the FCC main quadrupoles.

8 References

[1] M. Karppinen, "New Mechanical Concept for Nb3Sn Quadrupole", CERN-ACC-2014-0244.

[2] M. Karppinen et al., "Design of 11T Twin-Aperture Nb3Sn Dipole Demonstrator Magnet for LHC Upgrades", IEEE Trans. Appl. Supercond., Vol. 22, No. 3, June 2012

[3] M. Juncho, "Support Structure Design of the Nb3Sn Quadrupole for the high Luminosity LHC", ASC-14, Charlotte, August 2014.

[4] ROXIE, https://espace.cern.ch/roxie

[5] PITHIA BEM software package, www.feacomp.com/pithia

[6] C. Kokkinos et al., "The Short Model Coil (SMC) Nb3Sn Program: FE Analysis with 3D Modeling", IEEE Trans. Appl. Supercond., Vol. 22, No. 3, June 2012.

[7] ANSYS Mechanical APDL Element Reference, ANSYS Release 15.0, ANSYS Inc, November 2013.

[8] ANSYS Mechanical APDL Contact Technology Guide, ANSYS Release 15.0, ANSYS Inc, November 2013.

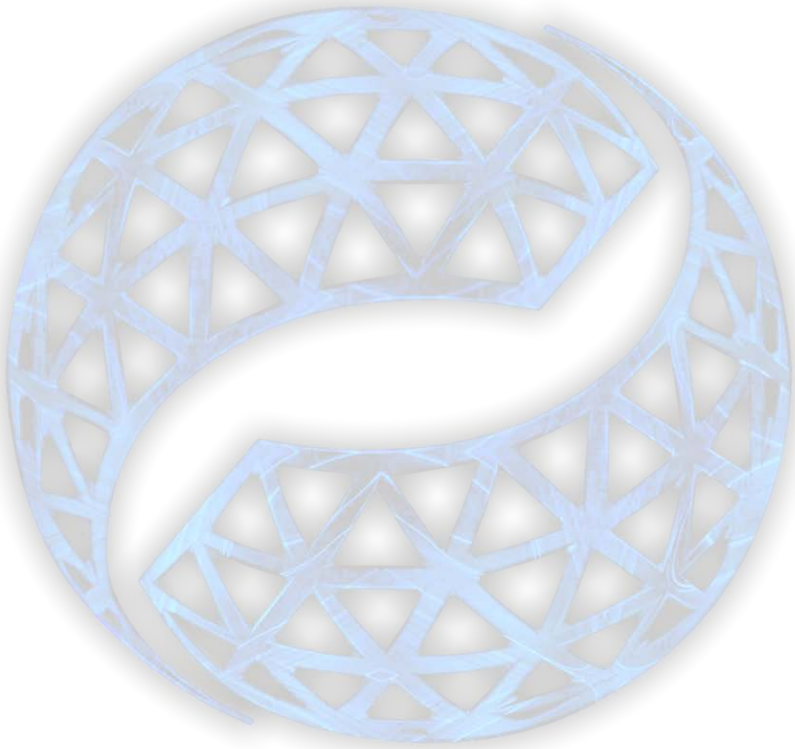

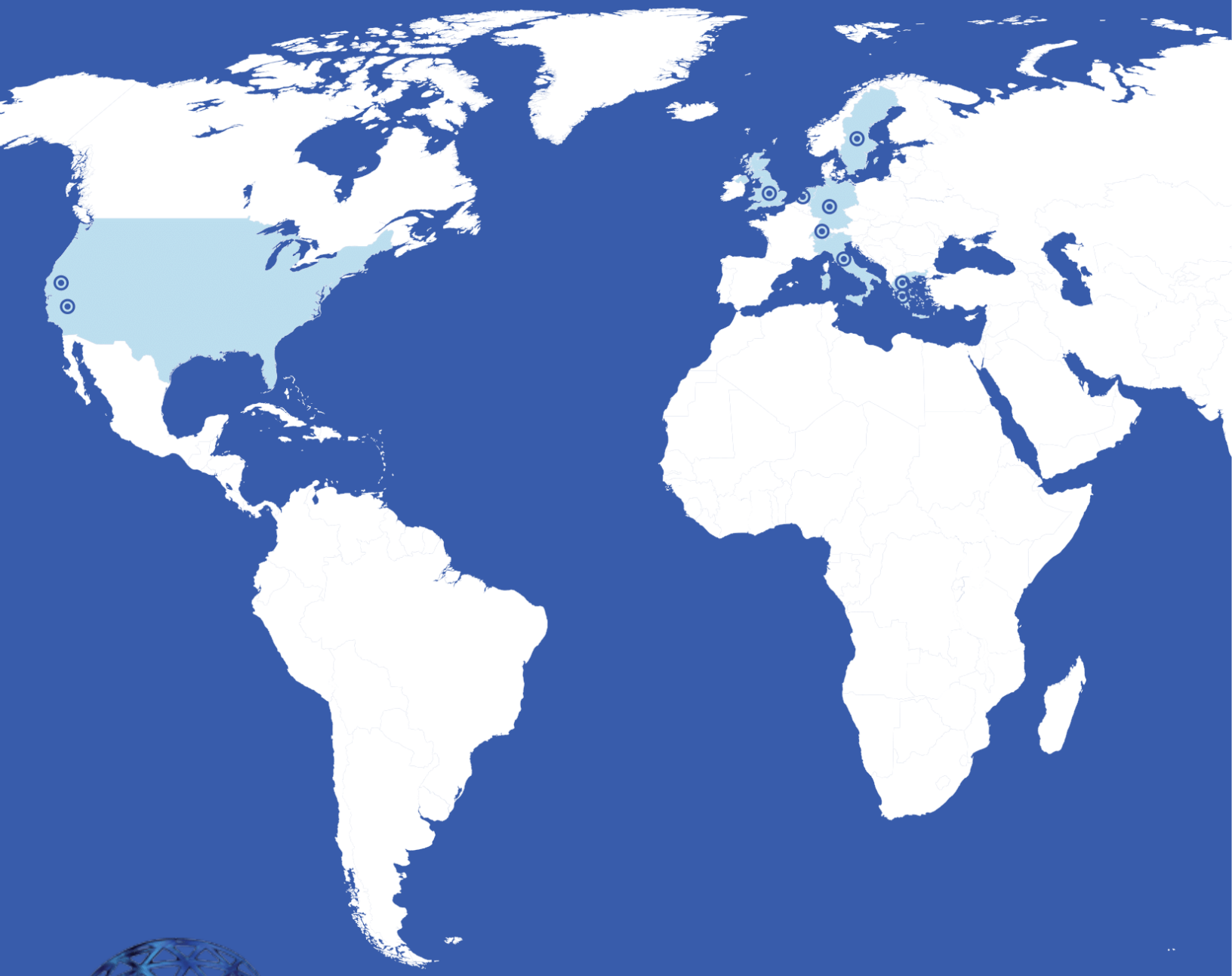

FEAC©

SIMULATION DRIVEN PRODUCT DEVELOPMENT

info@feacomp.com

www.feacomp.com